Combined Bulk and Surface Passivation in Dimensionally Engineered 2D-3D Perovskite Films via Chlorine Diffusion

Md Arafat Mahmud[*]*, Huyen T. Pham, The Duong, Yanting Yin, Jun Peng, Yiliang Wu, Wensheng Liang, Li Li, Anand Kumar, Heping Shen, Daniel Walter, Hieu T. Nguyen, Naeimeh Mozaffari, Grace Dansoa Tabi,, Gunther Andersson, Kylie R. Catchpole, Klaus J. Weber, and Thomas P. White**

Dr. M. A. Mahmud
School of Engineering, The Australian National University, Canberra, ACT 2601, Australia
School of Physics, University of Sydney, NSW 2006, Australia
E-mail: md.mahmud@sydney.edu.au, thomas.white@anu.edu.au

Dr. T. Duong, Dr. J. Peng, Dr. Y. Wu, Dr. W. Liang, Dr. H. Shen, Dr. D. Walter, Dr. H. T. Nguyen, N. Mozaffari, G. D. Tabi, Prof. K. R. Catchpole, Prof. K. J. Weber, Dr. T. P. White
School of Engineering, The Australian National University, Canberra, ACT 2601, Australia

Huyen T. Pham
Department of Electronic Materials Engineering, Research School of Physics, Australian National University, Canberra, ACT 2601, Australia

Dr Li Li
Australian National Fabrication Facility (ANFF)
Department of Electronic Materials Engineering, The Australian National University, Canberra, ACT, 2601 Australia

Dr. Y. Yin, Anand Kumar, Prof. G. Andersson
Flinders Institute for Nanoscale Science and Technology, Flinders University, Adelaide SA 5042, Australia
Flinders Microscopy and Microanalysis, College of Science and Engineering, Flinders University, Adelaide, SA 5042, Australia

Keywords: mixed dimensional perovskite, bulk passivation, surface passivation, Cl diffusion

Abstract:

Dimensional engineering of perovskite films is a promising pathway to improve the efficiency and stability of perovskite solar cells (PSCs). In this context, surface or bulk passivation of defects in 3D perovskite film by careful introduction of 2D perovskite plays a key role. Here we demonstrate a 2D perovskite passivation scheme based on octylammonium chloride, and show that it provides both bulk and surface passivation of 1.6eV bandgap 3D perovskite film for highly efficient (~23.62%) PSCs with open-circuit voltages up to 1.24V. Surface and depth-

resolved microscopy and spectroscopy analysis reveal that the Cl^- anion diffuses into the perovskite bulk, passivating defects, while the octylammonium ligands provide effective, localized surface passivation. We find that the Cl^- diffusion into the perovskite lattice is independent of the 2D perovskite crystallization process and occurs rapidly during deposition of the 2D precursor solution. The annealing-induced evaporation of Cl from bulk perovskite is also inhibited in 2D-3D perovskite film as compared to pristine 3D perovskite, ensuring effective bulk passivation in the relevant film.

1. Introduction

Perovskite solar cells (PSCs) are considered as a potential breakthrough photovoltaic (PV) technology due to their high power conversion efficiency (PCE) and low-cost fabrication potential.[1] The independently certified PCE of PSCs has already reached 25.5%,[1a] and there are multiple avenues yet to be explored to further enhance performance.[2] In particular, state-of-the-art PSCs are still limited by trap-assisted carrier recombination that reduces the open-circuit voltage (V_{OC}), and hence the PCE.[3] Therefore, substantial research efforts have focused on bulk and surface passivation schemes for perovskite films and interfaces between the perovskite and the charge transport layers, respectively.[4]

Among the reported strategies, dimensional engineering of perovskite films can reduce both bulk and surface recombination losses[5] while also improving the moisture stability of PSCs.[5c, 5d, 5g-l, 5n, 5p] Dimensional engineering refers to the introduction of one or multiple large alkyl or arylammonium cations (termed as spacer or interlayer cations) into the A-site of a three-dimensional (3D) ABX_3 perovskite crystal (A: organic or inorganic cations, B: divalent metal cations, X: halide anions), which transforms the 3D crystal lattice into a two-dimensional (2D) or quasi-2D layered structure.[6] For dimensionally engineered or mixed dimensional 2D-3D perovskite films, the spacer cations can either be incorporated into the bulk of perovskite[5h, 5j, 5k, 7] or on top[5a-g, 5i, 5l-n, 5p, 8] or both sides[5e, 6b] of the perovskite active layer. Most reports of

bulk incorporated 2D perovskite have attributed passivation effects to the preferential formation of 2D perovskite phases at the 3D perovskite grain boundaries, and a consequent reduction in crystal defects in these regions.[5h, 9] On the other hand, ultra-thin 2D perovskite films or unreacted spacer cation compounds applied to the surface of 3D perovskite films can chemically-passivate undercoordinated Pb atoms[10] or other interfacial defects at the perovskite-transport layer interfaces, improving both V_{oc} and PCE.[5a-g, 5i, 5l-n, 5p, 6b, 8] Therefore, combining the bulk and surface passivation benefits of dimensional engineering into a single processing step is an attractive and cost-effective strategy[11] to maximize mixed-dimensional PSC perfomance.

Recently, Zheng et al. demonstrated bulk incorporated oleylamine based 2D perovskite, where the large organic ligands are expelled to the 3D perovskite surface during the crystal growth stage.[12] The self-assembled oleylamine cations passivate interfacial trap-states between the perovskite and charge transport layers as well as defects in the perovskite bulk.[12] The reported surface passivation mechanism relies on the self-assembly of the spacer cations on the 3D perovskite surface during crystallization. Since the bulky organic cations are generally less mobile than the other organic or inorganic cations in the A-site,[5k, 7e] this diffusion and self-assembly approach to achieve both bulk and surface passivation is unlikely to work for all spacer cations. As an alternative approach, here we combine the concepts of dimensional engineering and anion engineering to select a 2D perovskite precursor compound that can simultaneously passivate surface and bulk defects when applied to the surface of a 3D perovskite film. The rationale for this strategy comes from the recent demonstration of anion engineering with mixed dimensional perovskite films for bulk perovskite passivation and film quality enhancement.[13]

Most previous studies of surface passivation with 2D perovskite forming cations have used iodide or bromide-based precursor compounds (eg: butylammonium iodide, butylammonium bromide), as these are the dominant halide components in most 3D perovskite films. It is not

necessary, however, to limit the anion choice to I^- and Br^-. In fact, Cl^- is a promising anion candidate for a number of reasons: (i) Cl^- having a small ionic radius can easily diffuse into the bulk perovskite matrix from perovskite surface,[7e] (ii) Diffused Cl^- can easily be accommodated at the vacant lattice sites of mixed-composition 3D perovskite,[14] which are created by the migration of other halide anions in the perovskite matrix and/or the evaporation of volatile organic cations,[15] and (iii) Cl^- forms a stronger bonding with Pb than I in the perovskite lattice, which is beneficial to bulk defect passivation.[7e] Therefore, replacing I^- or Br^- [5a, 5d, 5j] with Cl^- in the 2D perovskite precursor offers the possibility of bulk passivation in parallel with the surface passivation provided by the bulky cation. We note that Cl^- based precursor compounds have been used for bulk 2D perovskite incorporation,[16] however this approach does not offer any surface passivation so the device performance was relatively low.

In this work, we apply a Cl^- based 2D perovskite precursor compound on the perovskite/hole transport layer interface of a PSC to achieve simultaneous surface and bulk passivation, resulting in an average device PCE of 23.4%, and a champion PCE of 23.6%. These dimensionally engineered PSCs achieve V_{OC} values as high as 1.24 V using 3D perovskite absorbers with an optical bandgap of ~1.6 eV. We chose $C_8H_{20}IN^+$ [octylammonium (OA)] as the interlayer cation, which is commonly combined with I^- or Br^- anions to form a highly effective 2D perovskite passivation layer.[5b, 5c, 5p, 17] X-Ray diffraction (XRD), depth profiling microscopy and spectroscopy characterization reveal that Cl^- anions diffuse into the 3D perovskite lattice and occupy vacant lattice sites in the perovskite matrix leading to effective bulk passivation, while the large organic ligands provide excellent surface passivation. We further demonstrate that the Cl^- diffusion process is independent of the post-deposition annealing step for the crystallization of 2D perovskite film and the diffusion occurs rapidly as the spacer-cation-compound precursor is deposited on the 3D perovskite film.

2. Results and Discussion

To assess the role of the precursor halide in 2D perovskite passivation, we fabricated PSCs incorporating 2D perovskite surface layers on 3D perovskite films using OAI, OABr and OACl, respectively. Control devices with no 2D perovskite suface layer were also fabricated. The 2D-3D perovskite devices are termed as OAI, OABr and OACl PSCs for the remainder of the discussion. To optimize the 2D perovskite precursor concentration, three different concentrations of each compound were used to fabricate PSCs (Figures S1-S3). The thin-film layer sequence of the fabricated PSCs was: FTO/compact TiO_2 (~70 nm)/mesoporous TiO_2 (~80 nm)/poly(methyl methacrylate): phenyl-C60-butyric acid methyl ester (PMMA:PCBM) (<5 nm)[18]/$Cs_{0.07}Rb_{0.03}FA_{0.765}MA_{0.135}PbI_{2.55}Br_{0.45}$ perovskite (~500 nm)/OAI, OABr or OACl (maximum ~10 nm)/Spiro-OMeTAD (~180 nm)/Au (80 nm) (Figure 1a), where MA and FA denote methylammonium (CH_3NH_3) and formamidinium [$HC(NH_2)_2$], respectively. Representative scanning electron microscopy (SEM) cross-section images of each device (including the control) are presented in Figure S4 showing the constituent layers. We do not observe any distinct 2D perovskite layer in the OAI, OABr or OACl PSCs from the SEM images, however transmission electron microscopy (TEM) (Figure 2) cleary shows characteristic lattice spacings of 2D and 3D perovskite at the interface. We also note that the 2D perovskite layers are non-uniform and discontinuous as previously observed in PSCs using butylammonium-based 2D passivation layers.[5e, 19] Metastable impact electron spectroscopy (MIES) was also performed on the sample surfaces to detect the electronic properties and composition. MIES is a surface sensitive method that is ideal for characterizing only the outermost layer of a sample.[19-20] Figure S5(a) shows the MIE spectra of the control and the three OA(I,Br,Cl) based passivated samples. The spectra of the passivated samples are all similar and include contributions from both the 2D and 3D perovskite components, which can be identified using singular value decomposition (SVD). Figure S5(b,c) show reference spectra and weighting factors for the two spectral components extracted from SVD. The spectra of all three passivated samples contain a significant fraction (~30%) of the reference (bulk 3D

perovskite) component, indicating that the outermoster layer contains a mixture of both 2D and 3D perovskite material. This is further evidence that the passivation layer is discontinous on the surface of the underlying 3D perovskite film.

The optimum precursor concentration of OAI, OABr and OACl for maximum PSC efficiency is found to be 2 mg/ml. At higher precursor concentrations the short-current density (J_{SC}) and fill-factor (FF) are reduced, consistent with increased charge transport resistance due to a thicker semi-insulating surface layer of 2D perovskite.[5e, 5g] The photovoltaic parameters of control and passivated 2D-3D PSCs (at optimum concentration) are presented in Figures 1b-1e. All three passivated PSC variations exhibit higher PCE than the control cells, with the OACl devices having the highest average efficiency. Figures 1b-1e show that the PCE improvement in the OACl devices is due to a higher V_{OC} and slightly increased FF, while the J_{SC} remains comparable for all device types. The enhanced V_{OC} in OACl devices indicates a reduction in non-radiative recombination losses, which we discuss in the following sections. Figure 3a shows the current density-voltage (J-V) curves of the best performing control, OAI, OABr and OACl PSCs measured in the reverse scan direction (V_{oc} to J_{sc}). J-V curves of all the PSCs for both forward and reverse scans are presented in Figure S6 and the performance parameters are summarized in Table 1. All of the PSCs exhibit negilible photocurrent hysteresis at the 50mV/s scan rate used here. This is expected due to the PMMA:PCBM passivation layer[18] at the electron transport layer (ETL)/perovskite interface.

The best-performing OACl device achieved a PCE of 23.6% (in reverse scan) with a remarkable V_{OC} of 1.24 V. The same cell also had the highest steady state efficiency (~23.4%; held at maximum power point voltage (V_{MPP}) for 100 seconds) of all the devices, compared to 20.6% for the control, 22.6% for OAI and 23.0% for OABr PSCs (Figure 3b). We observe a slight blue-shift in the external quantum efficiency (EQE) spectra for OACl and OABr devices,

however the integrated J_{SC} values are comparable to the control and OAI devices (Figure 3c), which is consistent with the J-V measurements.

To investigate the superior performance of OACl PSCs we conducted a series of optical, structural and electronic measurements on both films and devices. Steady-state photoluminescence (PL) measurements of perovskite films on ETL/FTO/glass substrates (Figure 4a) show the highest PL intensity for OACl treated films, followed by OABr, OAI and control films, respectively. This is consistent with the V_{OC} values in complete devices and confirms that the OACl treatment provides the most effective passivation. There was also a small blue-shift in the peak PL emission wavelength for OACl and OABr films compared to OAI and control perovskite films (inset of Figure 4a), which is similar to the trend observed in the EQE curves. No short-wavelength PL emission was observed from the high band-gap 2D perovskite due to the low precursor concentrations used here, similar to previous studies.[5a, 5g, 19] The steady-state PL measurements were complemented by PL imaging of complete PSCs measured under open-circuit conditions (Figures 4b-4e). As expected, the OACl device exhibits the highest PL emission, followed by OABr, OAI and control devices. The PL intensity also increases with higher precursor concentration due to the thicker passivation layer (Figure S7), which is consistent with the increased V_{OC} in corresponding devices. These results support the conclusion that OACl based 2D perovskite is more effective at reducing non-radiative charge recombination compared to OAI or OABr based 2D perovskite films.

To further investigate the interfacial interactions with 2D passivation layers, we used Fourier-transform infra-red (FTIR) spectroscopy to probe unpassivated control and 2D passivated films deposited on silicon substrates (Figure 5a). All of the films show characteristic FTIR peaks of 3D perovskite,[21] but the OAI, OABr and OACl films exhibit additional $–CH_2$ stretching vibration (symmetric and asymmetric) and $–CH_3$ stretching vibration (asymmetric) peaks in the 2850-3000 cm^{-1} wavenumber region, related to OA^+ cations (inset of Figure 5a).[21a-c] Deconvolution of high-resolution scans of C 1s and N 1s with X-ray photoelectron spectroscopy

(XPS) (Figure S8) also show an increase in the weighting factor of C (C-C/CH_3) and N (NH_3^+) for OAI, OABr and OACl films relative to the control (Figure 5b), indicating the presence of the large organic ligand cations (OA^+ cations) in all passivated films.

The role of OA^+ cations in surface passivation has been well-studied in previous literature,[5b, 5c, 5p, 17] so we instead focus here on the precursor halide anion to understand why the OACl passivated films outperform both the OABr or OAI films. Scanning electron microscopy (SEM) imaging (Figure S9) shows no significant dependence of grain size or surface morphology on the 2D precursor halide, suggesting that the improved cell performance cannot be attributed to such large scale structural changes. Crystallographic changes due to the application of 2D perovskite surface layer were next probed with X-Ray Diffraction (XRD) measurements (Figure 5c). All the passivated films display an additional (020) 2D perovskite peak along with the characteristic (110) and (220) diffraction peaks of 3D perovskite. However, the (110) diffraction peak in the OACl treated film is clearly shifted (by ~0.1^0) to a higher diffraction angle with respect to the control film (inset of Figure 5c). OABr and OAI films also demonstrate peak-shifts (to higher and lower angles relative to the control by ~0.01^0, respectively), but these are much smaller than the shift observed for the OACl film. The shift of the (110) peak to a higher diffraction angle in the OACl film (relative to the control film) denotes a reduction in the unit cell volume, most likely due to the replacement of other halide anions (I^-, Br^-) or organic (MA^+ or FA^+) cations at their lattice sites with smaller-sized Cl^-.[14-15] We also observe a small blue-shift at the band-edge of the absorption curve for OACl film (Figure S10) corresponding to an increase in the optical bandgap (~0.01 eV) compared to control film (Figure 5b). This is also consistent with the small blue-shift in steady-state PL peak position for OACl perovskite film and EQE curves for OACl devices, as compared to control film and respective PSC. The OABr perovskite film also shows a slight increase in the optical bandgap (relative to control), but it is less prominent than OACl film. We note that these optical bandgap changes do not vary

significantly with the precursor concentration, at least for the concentration range used in our study (Figure S11).

The EQE, XRD and absorbance measurements all indicate the likely presence of Cl^- in the bulk and/or surface of the passivated perovskite films. To investigate this further we use surface and depth profiling XPS and energy-dispersive X-ray spectroscopy (EDX) measurements. From surface XPS characterization of the perovskite films, we find the relative concentration of Cl in OACl films is 2%, confirming the presence of Cl^- at the film surface (Figure 5e). As expected, no Cl is detected in the control, OAI or OABr perovskite films. This result was confirmed with surface SEM-EDX measurements which clearly detect the presence of Cl on the surface of OACl treated films (Figure 6), while the signal for Cl is below the EDX detection limit in other samples (Figures S12-S14).

Having confirmed the presence of Cl on the surface of the OACl treated films, we next investigate the depth distribution profile. Angle-resolved XPS (ARXPS) confirms the presence of Cl in the outer surface layer (up to 10 nm from surface) of OACl films (Figure S15), but this is too shallow to confirm signfiicant Cl penetration into the bulk (noting from the TEM image in Figure 2 that the passivation layer is up to 20nm thick in some places). The analysis of ARXPS illustrated that the NH_3^+ cation is enriched at the surface, which supports the presense of OA ions of the three samples. Of the OA compounds, the OAI had the strongest tendency to go to the the surface followed by Br^- and Cl^-. This finding supports the observation that Cl goes more into the bulk. We therefore conducted cross-sectional SEM-EDX of OACl and control perovskite films (Figure 7 and Figure S16) to obtain compositional data through the entire film. Figure 7 clearly demonstrates the uniform distribution of Cl in the bulk of OACl perovskite film, while no Cl is detected in the control film as expected (Figure S16). These results provide strong evidence that Cl^- anions from the OACl surface passivation treatment diffuse throughout the bulk of 3D perovskite film where they can passivate halide and/or organic cation lattice vacancies,[14-15] thereby reducing trap-induced charge carrier recombination. Thus, the OACl

treatment provides concurrent surface (courtesy of the OA-cation based 2D perovskite layer) and bulk (due to lattice vacancy filling by Cl^- anions) passivation, reflected in the improved V_{OC} and device performance of OACl PSCs.

The above results clearly demonstrate the complementary passivation roles of the Cl^- and OA^+ components of the 2D passivation layer precursor. We next investigate whether the formation of the 2D perovskite layer is necessary to observe the bulk passivation contribution from the Cl^-. In all of the results presented above, the passivated samples were annealed at ~100 ^{0}C to convert the OA spacer cation compound into a 2D perovskite surface layer.[5a, 5d] Although a small amount of 2D perovskite appears to be formed in unannealed samples (see TEM images in Figure S17), the annealing step is necessary to form sufficient 2D material to provide effective surface passivation. [5d, 5g, 5o] Whether this thermal treatment affects Cl^- diffusion into the bulk film an important consideration for process optimization.[7e] To probe this, we conducted cross-section SEM-EDX characterization of a PSC incorporating unannealed OACl perovskite film (Figure S18). The Cl distribution profile in the unannealed sample is comparable to that of the annealed sample (Figure 7). Therefore, we conclude that Cl^- diffusion occurs readily at room temperature following the application of the OACl compound to the 3D perovskite surfacce and therefore the passivation of bulk defects by Cl^- is largely independent of the 2D perovskite crystallization process. However, the annealing step is required for 2D perovskite formation and the associated surface passivation.

Some earlier studies of Cl based additives in bulk perovskite reported that Cl evaporated in the form of MA^+ ion and FACl (due to decomposition of MACl) as the perovskite film is annealed.[5f, 22] In these studies, no Cl was detected in the annealed perovskite film.In contrast, our results show that it is possible to introduce Cl^- into the bulk 3D film after it has been formed, via a surface treatment, and that the Cl^- remains even after annealing and subsequent 2D perovskite crystallization. We propose that this post-processing approach is a more effective way to introduce small amounts of Cl^- into the perovskite bulk for the following reasons: (a) Cl

interdiffuses into 3D bulk perovskite readily as the spacer-cation precursor is deposited on the surface. The 3D perovskite crystallization happens even before this step (due to prior annealing of 3D perovskite film) and the subsequent annealing just crystallizes the 2D perovskite film on 3D perovskite. The evaporation of Cl from 3D perovskite generally happens during the annealing-induced crystallization stage of 3D perovskite fim.[5f, 22] Since, during the crystallization of 2D perovskite film, the bulk 3D perovskite film is already crystallized, the Cl evaporation does not happen during the second annealing step. (b) The Cl evaporation rate is dependent on the annealing temperature used for perovskite crystallization.[22] It has been previously reported that Cl can be present in perovskite bulk even with an annealing step of 100 ^{0}C (during 3D perovskite crystallization) and the Cl content only goes below the detection limit of spectroscopy when the 3D perovskite is annealed at 150 ^{0}C.[22] In line with the the finding of this study, the annealing temperature used in our work (~100 ^{0}C) does not induce evaporation of Cl from the perovskite bulk. (c) Bulky organic ligands have been reported to inhibit ionic motion at 2D/3D perovskite interface.[5k] Therefore, the Cl evaporation may be inhibited by the presence of large spacer cations on 3D perovskite surface.

We have also investigated the light-soaking stability of the fabricated PSCs by holding them at their maximum power point under continuous illumination (1 sun) in an inert atmosphere (Figure S19). After 70 hours of continuous light soaking, the OACl PSC demonstrated the best device stability, followed closely by OABr and OAI PSCs, respectively and the poorest device stability is exhibited by the control device. The enhanced device stability in OACl PSC may be due to the reduced defect density which has been shown to contribute to device performance degradation with aging.[23] The long-term PSC stability can further could be enhanced by replacing the hygroscopic Spiro-OMeTAD HTL with a novel, dopant-free HTL.[5n, 24]

3. Conclusion

In summary, we have demonstrated dimensional engineering of perovskite films using a Cl based spacer cation compound (OACl) that provides concurrent bulk and surface passivation for enhanced device performance. The dual passivation mechanism enabled a remarkable V_{OC} of 1.24 V and a champion cell efficiency of 23.6%. Our experimental results suggest that Cl^- anions from the spacer-cation compound diffuse into the bulk 3D perovskite film where they passivate lattice vacancy defects. We further demonstrate that the Cl diffusion occurs independently of the thermal annealing step that induces 2D perovskite crystallization. Such surface treatment approaches may be more effective for introducing Cl^- into bulk 3D perovskite films compared to bulk incorporation during 3D film formation. OACl based 2D-3D PSCs also demonstrate improved light-stability compared to unpassivated, control devices in an inert atmosphere. Further enhancement in device efficiency and lifetime can be attained by exploring anion composition engineering for mixed dimensional PSCs.

4. Experimental Section

Experimental details are provided in the Supporting Information section.

Supporting Information

Supporting Information is available from the Wiley Online Library or from the author.

Acknowledgements

The work was supported by the Australian Government through the Australian Renewable Energy Agency (ARENA) and the Australian Research Council (ARC). T.P.W is the recipient of an Australian Research Council Australian Future Fellowship (project number FT180100302) funded by the Australian Government. Responsibility for the views, information or advice herein is not accepted by the Australian Government. This work has been made possible through the access to the ACT Node of the Australian National Fabrication Facility (ANFF @ ANU) and the Australian Microscopy and Microanalysis Research Facility (AMMRF) at the Centre for Advanced Microscopy (CAM @ ANU).

Conflict of Interest

The authors declare no conflict of interest.

Received: ((will be filled in by the editorial staff))
Revised: ((will be filled in by the editorial staff))
Published online: ((will be filled in by the editorial staff))

References

[1] a) National Renewable Energy Laboratory (NREL) Efficiency Chart, https://www.nrel.gov/pv/cell-efficiency.html, accessed: 1 December, 2020; b) *Nature Energy* **2020**, 5, 1; c) L. Meng, J. You, Y. Yang, *Nature Communications* **2018**, 9, 5265.

[2] a) J. Chen, N.-G. Park, *ACS Energy Letters* **2020**, 5, 2742; b) N.-G. Park, *Advanced Energy Materials* **2020**, 10, 1903106.

[3] a) D. Luo, R. Su, W. Zhang, Q. Gong, R. Zhu, *Nature Reviews Materials* **2020**, 5, 44; b) H. Jin, E. Debroye, M. Keshavarz, I. G. Scheblykin, M. B. J. Roeffaers, J. Hofkens, J. A. Steele, *Materials Horizons* **2020**, DOI: 10.1039/C9MH00500E; c) S. Mahesh, J. M. Ball, R. D. J. Oliver, D. P. McMeekin, P. K. Nayak, M. B. Johnston, H. J. Snaith, *Energy & Environmental Science* **2020**, 13, 258.

[4] a) L. Fu, H. Li, L. Wang, R. Yin, B. Li, L. Yin, *Energy & Environmental Science* **2020**, 13, 4017; b) B. Chen, P. N. Rudd, S. Yang, Y. Yuan, J. Huang, *Chemical Society Reviews* **2019**, 48, 3842; c) F. Gao, Y. Zhao, X. Zhang, J. You, *Advanced Energy Materials* n/a, 1902650; d) S. Akin, N. Arora, S. M. Zakeeruddin, M. Grätzel, R. H. Friend, M. I. Dar, *Advanced Energy Materials* n/a, 1903090; e) J. Kim, A. Ho-Baillie, S. Huang, *Solar RRL* **2019**, 3, 1800302.

[5] a) Q. Jiang, Y. Zhao, X. Zhang, X. Yang, Y. Chen, Z. Chu, Q. Ye, X. Li, Z. Yin, J. You, *Nature Photonics* **2019**, DOI: 10.1038/s41566-019-0398-2; b) H. Min, M. Kim, S.-U. Lee, H. Kim, G. Kim, K. Choi, J. H. Lee, S. I. Seok, *Science* **2019**, 366, 749; c) H. Kim, S.-U. Lee, D. Y. Lee, M. J. Paik, H. Na, J. Lee, S. I. Seok, *Advanced Energy Materials* **2019**, 9, 1902740; d) S. Gharibzadeh, B. Abdollahi Nejand, M. Jakoby, T. Abzieher, D. Hauschild, S. Moghadamzadeh, J. A. Schwenzer, P. Brenner, R. Schmager, A. A. Haghighirad, L. Weinhardt, U. Lemmer, B. S. Richards, I. A. Howard, U. W. Paetzold, *Advanced Energy Materials* **2019**, 9, 1803699; e) M. A. Mahmud, T. Duong, Y. Yin, H. T. Pham, D. Walter, J. Peng, Y. Wu, L. Li, H. Shen, N. Wu, N. Mozaffari, G. Andersson, K. R. Catchpole, K. J. Weber, T. P. White, *Advanced Functional Materials* n/a, 1907962; f) M. Kim, G.-H. Kim, T. K. Lee, I. W. Choi, H. W. Choi, Y. Jo, Y. J. Yoon, J. W. Kim, J. Lee, D. Huh, H. Lee, S. K. Kwak, J. Y. Kim, D. S. Kim, *Joule* **2019**, 3, 2179; g) Y. Cho, A. M. Soufiani, J. S. Yun, J. Kim, D. S. Lee, J. Seidel, X. Deng, M. A. Green, S. Huang, A. W. Y. Ho-Baillie, *Advanced Energy Materials* **2018**, 8, 1703392; h) J.-W. Lee, Z. Dai, T.-H. Han, C. Choi, S.-Y. Chang, S.-J. Lee, N. De Marco, H. Zhao, P. Sun, Y. Huang, Y. Yang, *Nature Communications* **2018**, 9, 3021; i) Y. Liu, S. Akin, L. Pan, R. Uchida, N. Arora, J. V. Milić, A. Hinderhofer, F. Schreiber, A. R. Uhl, S. M. Zakeeruddin, A. Hagfeldt, M. I. Dar, M. Grätzel, *Science Advances* **2019**, 5, eaaw2543; j) Z. Wang, Q. Lin, F. P. Chmiel, N. Sakai, L. M. Herz, H. J. Snaith, *Nature Energy* **2017**, 2, 17135; k) Y. Bai, S. Xiao, C. Hu, T. Zhang, X. Meng, H. Lin, Y. Yang, S. Yang, *Advanced Energy Materials* **2017**, 7, 1701038; l) T. Ye, A. Bruno, G. Han, T. M. Koh, J. Li, N. F. Jamaludin, C. Soci, S. G. Mhaisalkar, W. L. Leong, *Advanced Functional Materials* **2018**, 28, 1801654; m) T. Zhao, C.-C. Chueh, Q. Chen, A. Rajagopal, A. K. Y. Jen, *ACS Energy Letters* **2016**, 1, 757; n) E. H. Jung, N. J. Jeon, E. Y. Park, C. S. Moon, T. J. Shin, T.-Y. Yang, J. H. Noh, J. Seo, *Nature* **2019**, 567, 511; o) T. Duong, H. Pham, T. C. Kho, P. Phang, K. C. Fong, D. Yan, Y. Yin, J. Peng, M. A. Mahmud, S.

Gharibzadeh, B. A. Nejand, I. M. Hossain, M. R. Khan, N. Mozaffari, Y. Wu, H. Shen, J. Zheng, H. Mai, W. Liang, C. Samundsett, M. Stocks, K. McIntosh, G. G. Andersson, U. Lemmer, B. S. Richards, U. W. Paetzold, A. Ho-Ballie, Y. Liu, D. Macdonald, A. Blakers, J. Wong-Leung, T. White, K. Weber, K. Catchpole, *Advanced Energy Materials* n/a, 1903553; p) J. J. Yoo, S. Wieghold, M. C. Sponseller, M. R. Chua, S. N. Bertram, N. T. P. Hartono, J. S. Tresback, E. C. Hansen, J.-P. Correa-Baena, V. Bulović, T. Buonassisi, S. S. Shin, M. G. Bawendi, *Energy & Environmental Science* **2019**, 12, 2192; q) M. A. Mahmud, T. Duong, J. Peng, Y. Wu, H. Shen, D. Walter, H. T. Nguyen, N. Mozaffari, G. D. Tabi, K. R. Catchpole, K. J. Weber, T. P. White, *Advanced Functional Materials* n/a, 2009164.

[6] a) B. V. Beznosikov, K. S. Aleksandrov, *Crystallography Reports* **2000**, 45, 792; b) T. D. Md Arafat Mahmud, Yanting Yin, Jun Peng, Yiliang Wu, Teng Lu, Huyen T. Pham, Heping Shen, Daniel Walter, Hieu T. Nguyen, Naeimeh Mozaffari, Grace Dansoa Tabi, Yun Liu, Gunther Andersson, Kylie R. Catchpole, Klaus J. Weber, and Thomas P. White, *Small* **2020**, Just Accepted (DOI: 10.1002/smll.202005022).

[7] a) C. Fei, M. Zhou, J. Ogle, D.-M. Smilgies, L. Whittaker-Brooks, H. Wang, *Journal of Materials Chemistry A* **2019**, 7, 23739; b) G. Liu, H. Zheng, X. Xu, S. Xu, X. Zhang, X. Pan, S. Dai, *Advanced Functional Materials* **2019**, 29, 1807565; c) S. Jin, Y. Wei, B. Rong, Y. Fang, Y. Zhao, Q. Guo, Y. Huang, L. Fan, J. Wu, *Journal of Power Sources* **2020**, 450, 227623; d) C.-T. Lin, J. Lee, J. Kim, T. J. Macdonald, J. Ngiam, B. Xu, M. Daboczi, W. Xu, S. Pont, B. Park, H. Kang, J.-S. Kim, D. J. Payne, K. Lee, J. R. Durrant, M. A. McLachlan, *Advanced Functional Materials* **2020**, 30, 1906763; e) Z. Huang, A. H. Proppe, H. Tan, M. I. Saidaminov, F. Tan, A. Mei, C.-S. Tan, M. Wei, Y. Hou, H. Han, S. O. Kelley, E. H. Sargent, *ACS Energy Letters* **2019**, 4, 1521; f) A. A. Sutanto, N. Drigo, V. I. E. Queloz, I. Garcia-Benito, A. R. Kirmani, L. J. Richter, P. A. Schouwink, K. T. Cho, S. Paek, M. K. Nazeeruddin, G. Grancini, *Journal of Materials Chemistry A* **2020**, 8, 2343; g) E. Shirzadi, A. Mahata, C. Roldán Carmona, F. De Angelis, P. J. Dyson, M. K. Nazeeruddin, *ACS Energy Letters* **2019**, 4, 2989; h) J. Lu, L. Jiang, W. Li, F. Li, N. K. Pai, A. D. Scully, C.-M. Tsai, U. Bach, A. N. Simonov, Y.-B. Cheng, L. Spiccia, *Advanced Energy Materials* **2017**, 7, 1700444; i) H. Ren, S. Yu, L. Chao, Y. Xia, Y. Sun, S. Zuo, F. Li, T. Niu, Y. Yang, H. Ju, B. Li, H. Du, X. Gao, J. Zhang, J. Wang, L. Zhang, Y. Chen, W. Huang, *Nature Photonics* **2020**, DOI: 10.1038/s41566-019-0572-6; j) Y. Wang, H. Xu, F. Wang, D. Liu, H. Chen, H. Zheng, L. Ji, P. Zhang, T. Zhang, Z. D. Chen, J. Wu, L. Chen, S. Li, *Chemical Engineering Journal* **2019**, DOI: https://doi.org/10.1016/j.cej.2019.123589123589; k) S. Chen, N. Shen, L. Zhang, W. Kong, L. Zhang, C. Cheng, B. Xu, *Journal of Materials Chemistry A* **2019**, 7, 9542; l) S. Chen, N. Shen, L. Zhang, L. Zhang, S. H. Cheung, S. Chen, S. K. So, B. Xu, *Advanced Functional Materials* n/a, 1907759; m) J. Zhang, J. Qin, M. Wang, Y. Bai, H. Zou, J. K. Keum, R. Tao, H. Xu, H. Yu, S. Haacke, B. Hu, *Joule* **2019**, 3, 3061.

[8] T. Bu, J. Li, W. Huang, W. Mao, F. Zheng, P. Bi, X. Hao, J. Zhong, Y.-B. Cheng, F. Huang, *Journal of Materials Chemistry A* **2019**, 7, 6793.

[9] a) A.-F. Castro-Méndez, J. Hidalgo, J.-P. Correa-Baena, *Advanced Energy Materials* **2019**, 9, 1901489; b) T. Niu, J. Lu, M.-C. Tang, D. Barrit, D.-M. Smilgies, Z. Yang, J. Li, Y. Fan, T. Luo, I. McCulloch, A. Amassian, S. Liu, K. Zhao, *Energy & Environmental Science* **2018**, 11, 3358; c) Y. Liao, H. Liu, W. Zhou, D. Yang, Y. Shang, Z. Shi, B. Li, X. Jiang, L. Zhang, L. N. Quan, R. Quintero-Bermudez, B. R. Sutherland, Q. Mi, E. H. Sargent, Z. Ning, *Journal of the American Chemical Society* **2017**, 139, 6693; d) D. H. Cao, C. C. Stoumpos, O. K. Farha, J. T. Hupp, M. G. Kanatzidis, *Journal of the American Chemical Society* **2015**, 137, 7843; e) R. L. Milot,

R. J. Sutton, G. E. Eperon, A. A. Haghighirad, J. Martinez Hardigree, L. Miranda, H. J. Snaith, M. B. Johnston, L. M. Herz, *Nano Letters* **2016**, 16, 7001.
[10] H. Xu, G. Liu, X. Xu, S. Xu, L. Zhang, X. Chen, H. Zheng, X. Pan, *Solar RRL* **2020**, 4, 2000647.
[11] N. L. Chang, J. Zheng, Y. Wu, H. Shen, F. Qi, K. Catchpole, A. Ho-Baillie, R. J. Egan, *Progress in Photovoltaics: Research and Applications* **2021**, 29, 401.
[12] X. Zheng, Y. Hou, C. Bao, J. Yin, F. Yuan, Z. Huang, K. Song, J. Liu, J. Troughton, N. Gasparini, C. Zhou, Y. Lin, D.-J. Xue, B. Chen, A. K. Johnston, N. Wei, M. N. Hedhili, M. Wei, A. Y. Alsalloum, P. Maity, B. Turedi, C. Yang, D. Baran, T. D. Anthopoulos, Y. Han, Z.-H. Lu, O. F. Mohammed, F. Gao, E. H. Sargent, O. M. Bakr, *Nature Energy* **2020**, 5, 131.
[13] D. Kim, H. J. Jung, I. J. Park, B. W. Larson, S. P. Dunfield, C. Xiao, J. Kim, J. Tong, P. Boonmongkolras, S. G. Ji, F. Zhang, S. R. Pae, M. Kim, S. B. Kang, V. Dravid, J. J. Berry, J. Y. Kim, K. Zhu, D. H. Kim, B. Shin, *Science* **2020**, 368, 155.
[14] M. I. Saidaminov, J. Kim, A. Jain, R. Quintero-Bermudez, H. Tan, G. Long, F. Tan, A. Johnston, Y. Zhao, O. Voznyy, E. H. Sargent, *Nature Energy* **2018**, 3, 648.
[15] X. Liu, Z. Yu, T. Wang, K. L. Chiu, F. Lin, H. Gong, L. Ding, Y. Cheng, *Advanced Energy Materials* n/a, 2001958.
[16] M. S. de Holanda, R. Szostak, P. E. Marchezi, L. G. T. A. Duarte, J. C. Germino, T. D. Z. Atvars, A. F. Nogueira, *Solar RRL* **2019**, 3, 1900199.
[17] M. Jeong, I. W. Choi, E. M. Go, Y. Cho, M. Kim, B. Lee, S. Jeong, Y. Jo, H. W. Choi, J. Lee, J.-H. Bae, S. K. Kwak, D. S. Kim, C. Yang, *Science* **2020**, 369, 1615.
[18] J. Peng, Y. Wu, W. Ye, D. A. Jacobs, H. Shen, X. Fu, Y. Wan, T. Duong, N. Wu, C. Barugkin, H. T. Nguyen, D. Zhong, J. Li, T. Lu, Y. Liu, M. N. Lockrey, K. J. Weber, K. R. Catchpole, T. P. White, *Energy & Environmental Science* **2017**, 10, 1792.
[19] M. A. Mahmud, T. Duong, Y. Yin, J. Peng, Y. Wu, T. Lu, H. T. Pham, H. Shen, D. Walter, H. T. Nguyen, N. Mozaffari, G. D. Tabi, Y. Liu, G. Andersson, K. R. Catchpole, K. J. Weber, T. P. White, *Small* n/a, 2005022.
[20] a) Y. Yin, D. A. Lewis, G. G. Andersson, *ACS Applied Materials & Interfaces* **2018**, 10, 44163; b) A. R. M. Alharbi, J. M. Andersson, I. Köper, G. G. Andersson, *Langmuir* **2019**, 35, 14213.
[21] a) M. Slaný, Ľ. Jankovič, J. Madejová, *Applied Clay Science* **2019**, 176, 11; b) M. Jung, T. J. Shin, J. Seo, G. Kim, S. I. Seok, *Energy & Environmental Science* **2018**, 11, 2188; c) T. M. Koh, V. Shanmugam, X. Guo, S. S. Lim, O. Filonik, E. M. Herzig, P. Müller-Buschbaum, V. Swamy, S. T. Chien, S. G. Mhaisalkar, N. Mathews, *Journal of Materials Chemistry A* **2018**, 6, 2122; d) A. Solanki, M. M. Tavakoli, Q. Xu, S. S. H. Dintakurti, S. S. Lim, A. Bagui, J. V. Hanna, J. Kong, T. C. Sum, *Advanced Materials* **2020**, 32, 1907864; e) K. Hills-Kimball, Y. Nagaoka, C. Cao, E. Chaykovsky, O. Chen, *Journal of Materials Chemistry C* **2017**, 5, 5680; f) X. Guo, C. McCleese, C. Kolodziej, A. C. S. Samia, Y. Zhao, C. Burda, *Dalton Transactions* **2016**, 45, 3806; g) M. Acik, T. M. Alam, F. Guo, Y. Ren, B. Lee, R. A. Rosenberg, J. F. Mitchell, I. K. Park, G. Lee, S. B. Darling, *Advanced Energy Materials* **2018**, 8, 1701726.
[22] M. Mateen, Z. Arain, Y. Yang, X. Liu, S. Ma, C. Liu, Y. Ding, X. Ding, M. Cai, S. Dai, *ACS Applied Materials & Interfaces* **2020**, 12, 10535.
[23] a) C. M. Wolff, P. Caprioglio, M. Stolterfoht, D. Neher, *Advanced Materials* **2019**, 31, 1902762; b) J. Jiménez-López, E. Palomares, *Nanoscale* **2019**, 11, 20024.
[24] K. Rakstys, S. Paek, P. Gao, P. Gratia, T. Marszalek, G. Grancini, K. T. Cho, K. Genevicius, V. Jankauskas, W. Pisula, M. K. Nazeeruddin, *Journal of Materials Chemistry A* **2017**, 5, 7811.

Table:

Table 1: Photovoltaic parameters and hystereis index of the best-performing control, OAI, OABr and OACl PSCs from J-V characterization in both forward and reverse scan directions

Device	Champion /Average	Open-circuit Voltage (V_{OC}) (V)	Short-circuit Current Density (J_{SC}) (mA/cm^2)	Fill Factor (FF) (%)	Power Conversion Efficiency (PCE) (%)	Hysteresis Index (HI) $\left\|\frac{PCE_{REV} - PCE_{FOR}}{PCE_{REV}}\right\|$ (Champion Device)
Control	Champion (Reverse)	1.18	24.21	72.20	20.61	0.008
	Champion (Forward)	1.17	24.04	73.92	20.78	
	Average	1.18±0.004	24.12±0.1	72.96±1.07	20.7±0.1	
OAI	Champion (Reverse)	1.21	24.00	77.97	22.66	0
	Champion (Forward)	1.21	24.01	78.02	22.66	
	Average	1.21±0.001	23.98±0.03	78.24±0.39	22.7±0.1	
OABr	Champion (Reverse)	1.22	23.89	79.93	23.38	0.030
	Champion (Forward)	1.22	23.89	77.48	22.67	
	Average	1.22±0.004	24.16±0.1	78.71±0.6	23.1±0.2	
OACl	Champion (Reverse)	1.24	24.24	78.46	23.62	0.021
	Champion (Forward)	1.23	24.17	77.52	23.13	
	Average	1.23±0.009	24.13±0.1	78.64±1.2	23.4±0.2	

Figures:

Figure 1. a. Schematic of the thin film structure of control, OAI, OABr or OACl perovskite solar cells. Statistical distribution of experimental J-V parameters: b. distribution of PCE, c. distribution of V_{OC}, d. distribution of FF and e. distribution of J_{SC}. The data are based on the J-V results from 15 cells of each kind of device (scan direction: reverse scan, scan rate: 50 mV/s).

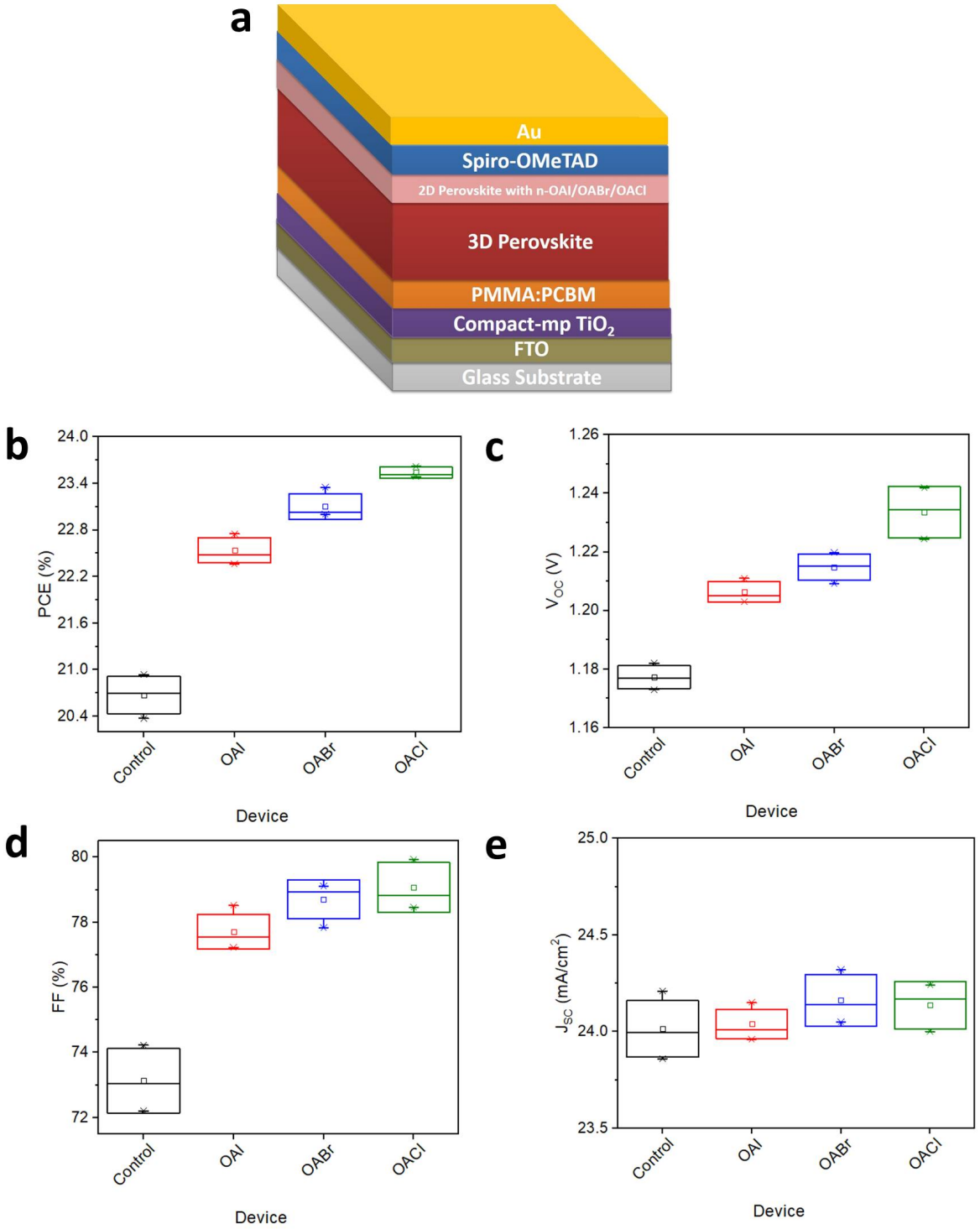

Figure 2. Cross-section transmission electron microscopy (TEM) image of OACl passivated device. (a) Full cross section, (b)-(c) higher magnification images showing 2D/3D perovskite interface, (d) higher magnification image showing the characteristic interplanar spacing of 2D and 3D perovskite at their interface.

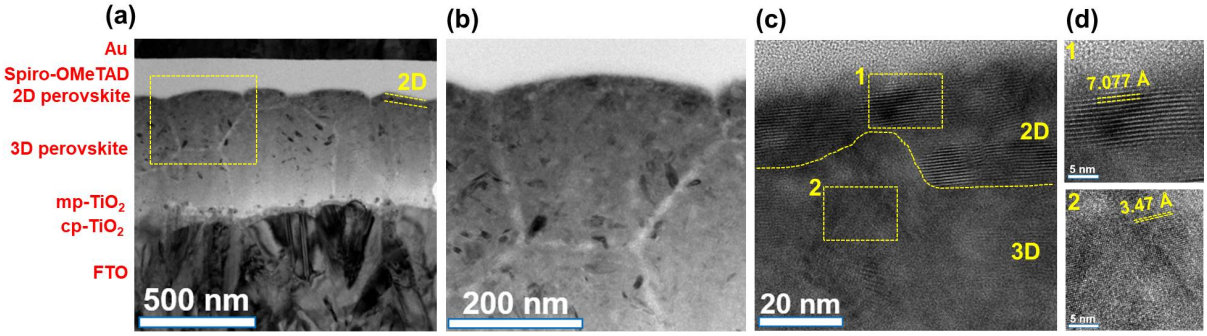

Figure 3. a. Current density-voltage (J-V) curves of the best performing control, OAI, OABr and OACl PSCs measured in reverse scan direction. b. Steady-state efficiency curves of control and 2D perovskite passivated PSCs at maximum power point. c. External quantum efficiency (EQE) curves of the corresponding devices.

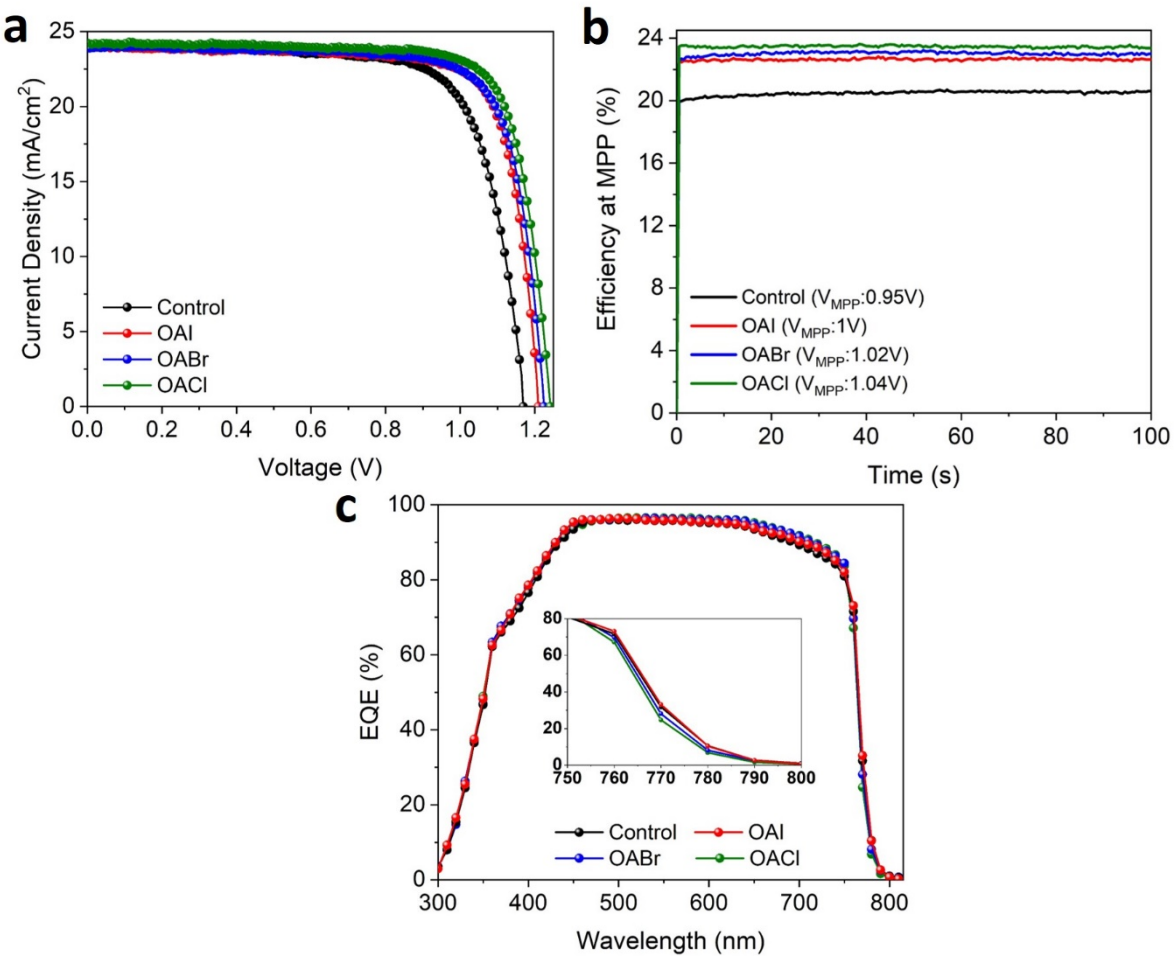

Figure 4. a. Steady-state PL spectra of control, OAI, OABr and OACl PSCs. PL images of b. control, c.OAI, d, OABr and e. OACl PSCs under open-circuit condition

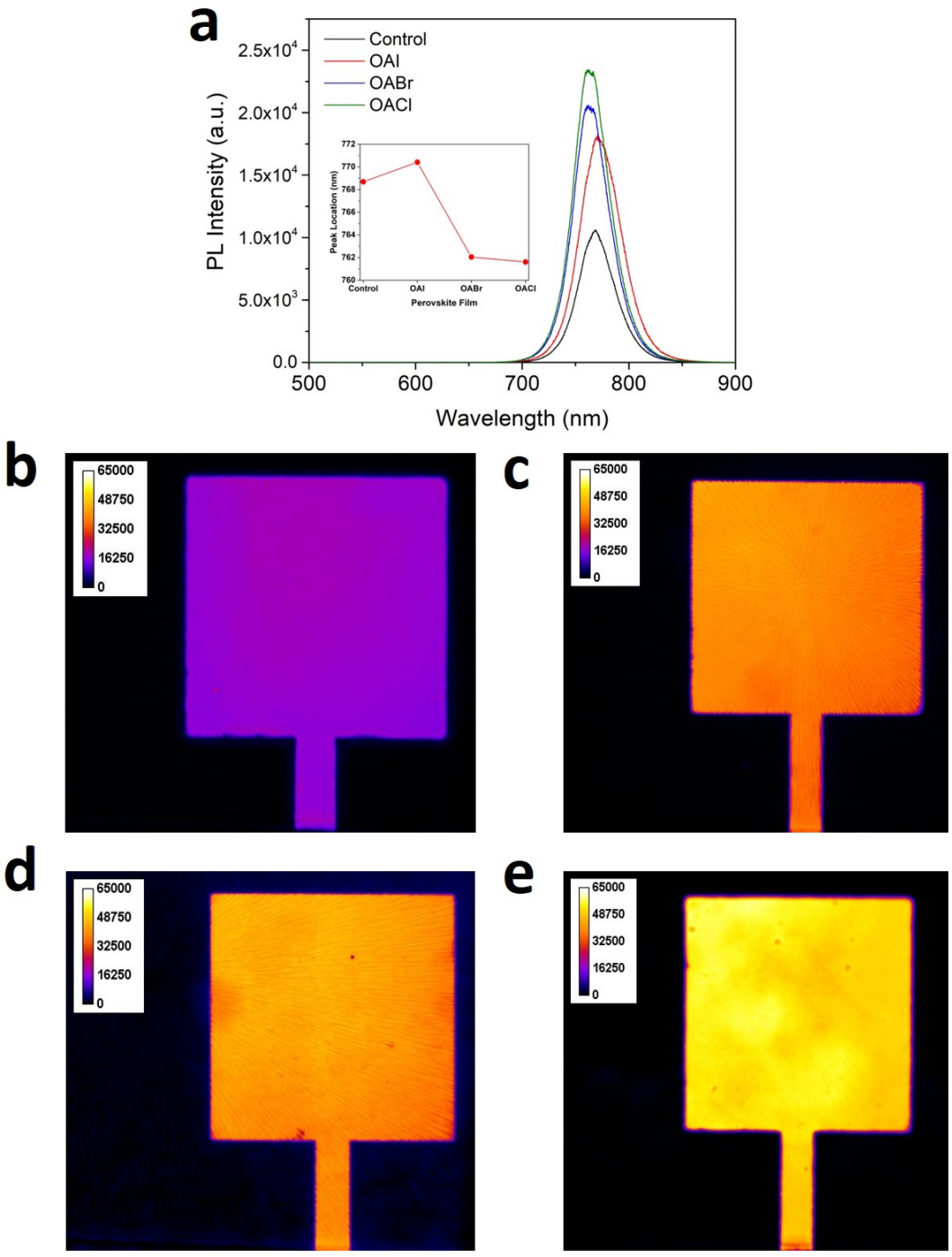

Figure 5. a. Fourier-transform infra-red (FTIR) spectra of control, OAI, OABr and OACl perovskite films (the inset demonstrates the characteristic peak of octylammonium cation), b. Relative intensity of C and N variables on control and 2D perovskite passivated films, calculated from the deconvolution of high-resolution C 1s XPS spectra, c. XRD diffraction patterns of perovskite films (the inset shows the shifts in diffraction angle of OAI, OABr and OACl perovskite films as compared to control), d. Tauc plots of the perovskite films showing the optical bandgap. e. Relative concentration of Cl on perovskite surface calculated from surface XPS measurement.

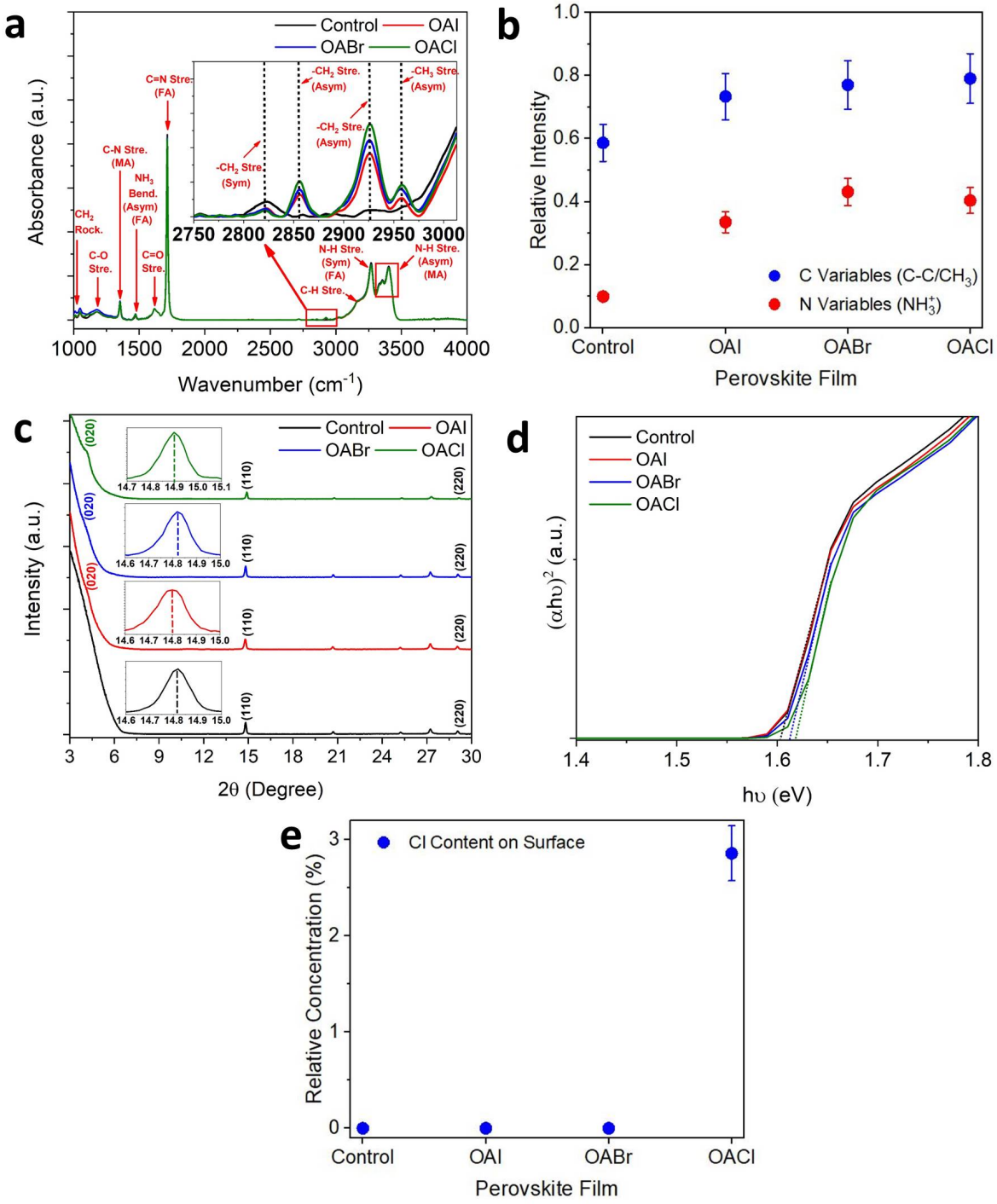

Figure 6. SEM-EDX mapping image of OACl passivated perovskite film, demonstrating the distribution of elements K, I, Br, Pb, Cs, Rb on the surface.

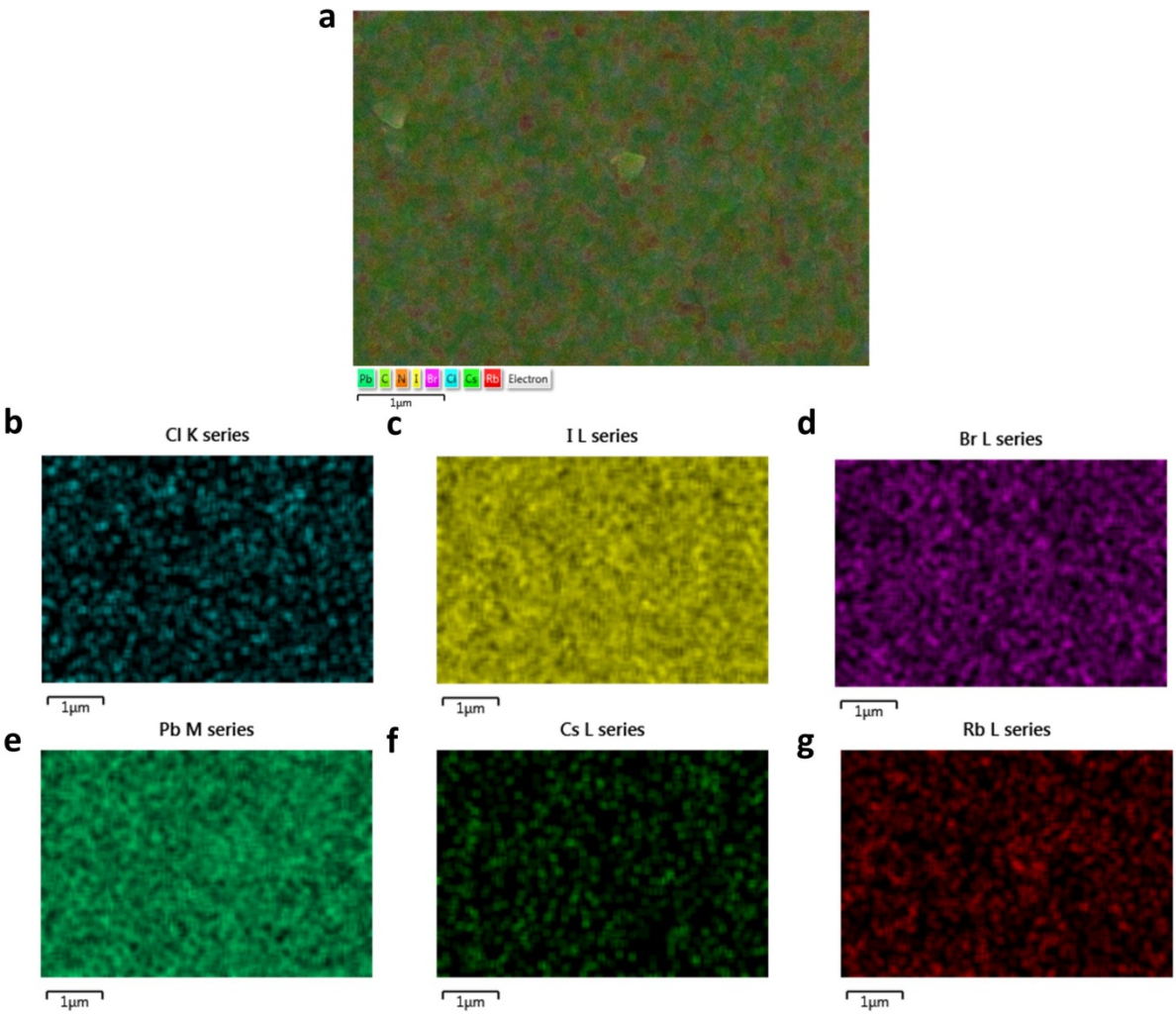

Figure 7. Cross-section SEM-EDX mapping image of OACl passivated perovskite solar cell, demonstrating the distribution of elements Pb, I, Cs Cl vertically through the device.

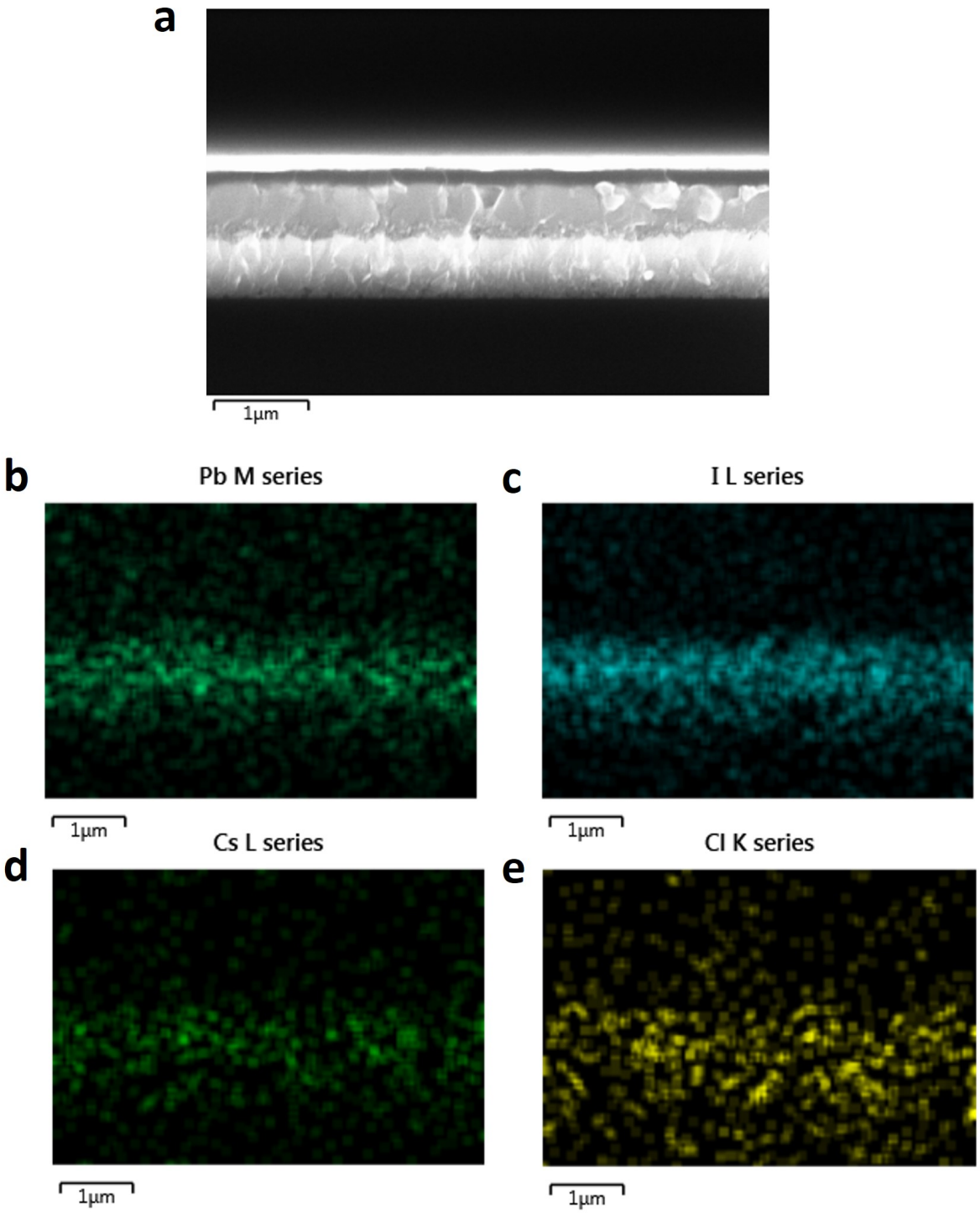

Table of Content Entry

Keywords: mixed dimensional perovskite, bulk passivation, surface passivation, Cl interdiffusion

Concurrent Bulk and Surface Passivation in Dimensionally Engineered 2D-3D Perovskite Films via Chlorine Interdiffusion

Md Arafat Mahmud[*]*, Huyen T. Pham, The Duong, Yanting Yin, Jun Peng, Yiliang Wu, Wensheng Liang, Li Li, Anand Kumar, Heping Shen, Daniel Walter, Hieu T. Nguyen, Naeimeh Mozaffari, Grace Dansoa Tabi,, Gunther Andersson, Kylie R. Catchpole, Klaus J. Weber, and Thomas P. White**

Supporting Information

Combined Bulk and Surface Passivation in Dimensionally Engineered 2D-3D Perovskite Films via Chlorine Diffusion

Md Arafat Mahmud[*]*, Huyen T. Pham, The Duong, Yanting Yin, Jun Peng, Yiliang Wu, Wensheng Liang, Li Li, Anand Kumar, Heping Shen, Daniel Walter, Hieu T. Nguyen, Naeimeh Mozaffari, Grace Dansoa Tabi,, Gunther Andersson, Kylie R. Catchpole, Klaus J. Weber, and Thomas P. White**

Supplementary Section

Experimental Section

a. Device Fabrication

FTO/glass substrates were sequentially cleaned with detergent, acetone, isopropanol, ethyl alcohol and deionized (DI) water for 10 minutes per step in an ultrasonic bath. They were then UV-ozone treated for 15 minutes. Next, a ~70 nm layer of cp-TiO_2 and a ~80 nm layer of mp-TiO_2 were deposited on the pre-cleaned substrates sequentially according to the processes described in Ref [1]. A thin PMMA:PCBM passivation layer was deposited on the substrate at a spin speed of 4000 rpm for 15 s with a ramp rate of 4000 rpm/s. Details regarding the preparation of PMMA:PCBM passivation solution can be found at Ref [2].

To prepare the control quadruple cation perovskite precursor, 1.1 M formamidinium iodide (Greatcell Solar), 0.2 M methyl ammonium bromide (Greatcell Solar), 0.2 M lead bromide (Greatcell Solar), 1.2 M lead iodide (Sigma Aldrich, 99%), 0.091 M cesium iodide (Sigma Aldrich, 99.999%) and 0.039 M rubidium iodide (Sigma Aldrich, 99.9%) were dissolved in 1 ml mixed solvent of *N,N*-dimethylformamide (DMF, Sigma Aldrich, Anhydrous, 99.8%) and dimethyl sulfoxide (DMSO, Sigma Aldrich, Anhydrous, 99.9%) with a volume ratio of 4:1. A two-step spin-coating program was used to coat the perovskite film on the substrates. Perovskite precursor solution was dropped onto the substrate, which was then rotated at 1000 rpm for 10 s with a ramp rate of 100 rpm/s and then at 4000 rpm for 25 s with a ramp rate of 1000 rpm/s. During the second step, ~150 µL of chlorobenzene (Sigma Aldrich, Anhydrous, 99.8%) was dropped on the center of the substrate 8 s prior to the end of the spinning program. Immediately after spin-coating, the substrates were placed on a hotplate and annealed for 30 minutes at 100 ^{0}C. For the passivated PSCs, OAI, OABr or OACl (Greatcell Solar) solution in 2-propanol (1 mg/ml, 2 mg/ml, 3 mg/ml) was prepared and spin-coated on the substrate (after the above 30 min annealing step) at 5000 rpm for 15 s with a ramp rate of 5000 rpm/s. This was followed by 10 minutes annealing on a hotplate at 100 ^{0}C.

For the HTL, Spiro-OMeTAD (LUMTEC) solution was prepared by dissolving 73.5 mg Spiro-OMeTAD in 1 ml chlorobenzene. The solution was doped with 17.5 µL of bis(trifluoromethane)sulfonimide lithium salt (Li-TFSI, Sigma Aldrich, 99.95% trace metal basis) (520 mg/mL in acetonitrile) and 28.5 µL of 4-tert-butylpyridine (Sigma Aldrich, 98%) to enhance the p-type conductivity. The Spiro-OMeTAD layer was spin-coated at 3500 rpm for 30 s with a ramp rate of 3500 rpm/s. The coated substrates were dried overnight in a humidity controlled box to ensure sufficient oxidation of the Spiro-OMeTAD film. The following day, a ~80 nm gold rear electrode was deposited on the coated substrates via thermal evaporation. The active area of the cell (0.165 cm^2) was defined using a shadow mask during the evaporation process.

All of the solution preparation, spin coating and annealing steps were carried out in a N_2 glovebox.

b. Device Measurement

i. J-V Measurement

J-V measurements were taken on a solar simulator system (Weblab Inc.) under 1 sun-condition (AM 1.5G, 1000 W/m^2, 25 ^{0}C). A certified Fraunhofer CalLab reference cell was used to calibrate the light intensity prior to the measurements. No preconditioning protocol was applied before the cell measurement. The cells were tested in a custom-built measurement jig under a flow of N_2 gas. For the forward and reverse scans, the voltage range was maintained at -0.1 V→1.25 V and 1.25 V→-0.1 V, respectively. Unless otherwise stated, all the measurements taken at a scan rate of 50 mV/s with a voltage step of 0.01 V.

ii. EQE Measurement

External quantum efficiency (EQE) measurements were performed in DC mode using a QEX10 spectral response system from PV measurements Inc.

c. Material Characterization

Optical characterization (transmittance, absorbance) of the films was conducted with a Perkin Elmer Lambda 1050 UV-vis-NIR spectrophotometer.

The surface morphology of perovskite films and cross-sectional SEM images of the PSC devices were captured from the FEI Verios SEM instrument at 2 kV acceleration voltage and 25 pA probe current. In addition, the Oxford electron dispersive X-ray spectrometer (EDS) with an 80mm^2 silicon drift detector integrated into this SEM system to explore the elemental composition of materials. The elemental mapping of perovskite solar cells was collected using Oxford EDS instrument at 20 kV and 0.8 nA for both surface and a cross-sectional view.

The cross-sectional sample of the perovskite solar cell was prepared by Helios NanoLab 600 Focus Ion Beam (FIB) milling. The microstructure of FIB-prepared lamellae was analysed by JEOL 2100F TEM instrument operated at 200 keV.

XRD characterization was conducted using a Bruker D2 phaser diffractometer operated at 30 kV, 10 mA at 2θ (Cu Kα) 10-80^0 with a step size of 2^0 and scan speed of 2.3^0/min.

The FTIR absorption spectra were measured on double-sided polished, silicon wafers with perovskite files deposited on one side, using a Bruker Vertex 80 V FTIR spectrometer with a resolution of 6 cm^{-1}.

For PL imaging, a custom-built PL imaging system, equipped with 430 nm royal-blue LEDs and 451/106 nm bandpass filters was used. The cells were held in a N_2-filled and temperature controlled custom-built jig and illuminated with a 1-sun equivalent intensity. A Peltier-cooled (-70 ^{0}C) Si CCD camera (Princeton Instruments Pixis 1024) along with a 750 nm long-pass filter was used to obtain a PL image of the cells with an exposure time of 0.01 s. The PL images were taken under both open-circuit and reverse bias (-1 V) conditions. Fiji software was used to subtract the open-circuit images from the reverse bias ones to ensure the PL emission was solely from the active area of the device.

For X-ray photoelectron spectroscopy (XPS) and UV light photoelectron spectroscopy (UPS) characterization, a SPECS (Berlin) machine was used. For XPS measurement, X-ray emission was conducted with Mg Kα line (12kV-200 W) anode from an UHV non-monochromatic source. High-resolution scans at a pass energy of 10 eV were recorded after a survey scan for characterizing the chemical states. The excitation energy was 1253.6 eV.

XPS can be conducted with certain angle of surface intersection [3]. In the work, the intersection angle between the sample surface and the electron path was 90º while the measuring depth was maximized. With the decrease of intersection angle, the electrons were not capable of reaching the sample surface due to the limits of the electron mean free path. Consequently, the measuring depth was diminished. In this work, intersection angles of 90º, 60°, 45° and 30° were used, correlating to probing depths up to approximately 10nm, 8.6nm, 7.1nm and 5nm, respectively. Identically the lower of the intersection angle used, the higher proportion of surface feature can be contributed to the spectra.

Metastable impact electron spectroscopy (MIES) [4] was performed in-situ with an excitation energy of 19.22 eV. MIES probes only the outermost layer of 0.2 nm of a sample surface, which provides information of the valence electronic states at the surface. By decomposing the spectra acquired from MIES and extrapolating the weighting factor of components with singular decomposition method (SVD) [5], the surface coverage of a sample can be derived.

All spectroscopy methods were applied in-situ in an ultra-high vacuum with a base pressure below 10^{-10} mbar. Further degradation and contamination of the samples can be excluded because the samples were not exposed to atmosphere during transfer.

Figure S1. Statistical distribution of J-V parameters in OAI PSCs for different concentrations: a. distribution of PCE, b. distribution of V_{OC}, c. distribution of FF and d. distribution of J_{SC}. The data are based on the J-V results from 15 cells of each kind of devices (scan direction: reverse scan, scan rate: 50 mV/s)

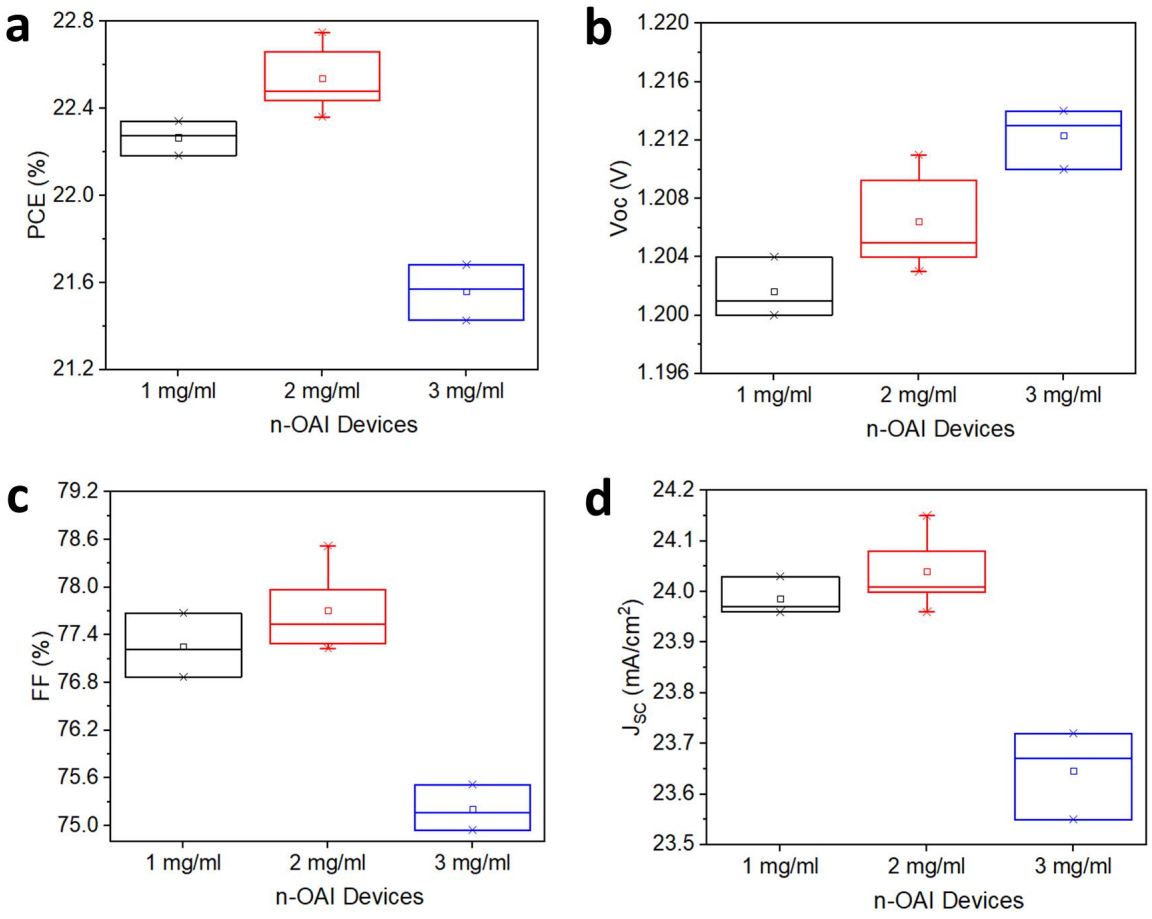

Figure S2. Statistical distribution of J-V parameters in OABr PSCs for different concentrations: a. distribution of PCE, b. distribution of V_{OC}, c. distribution of FF and d. distribution of J_{SC}

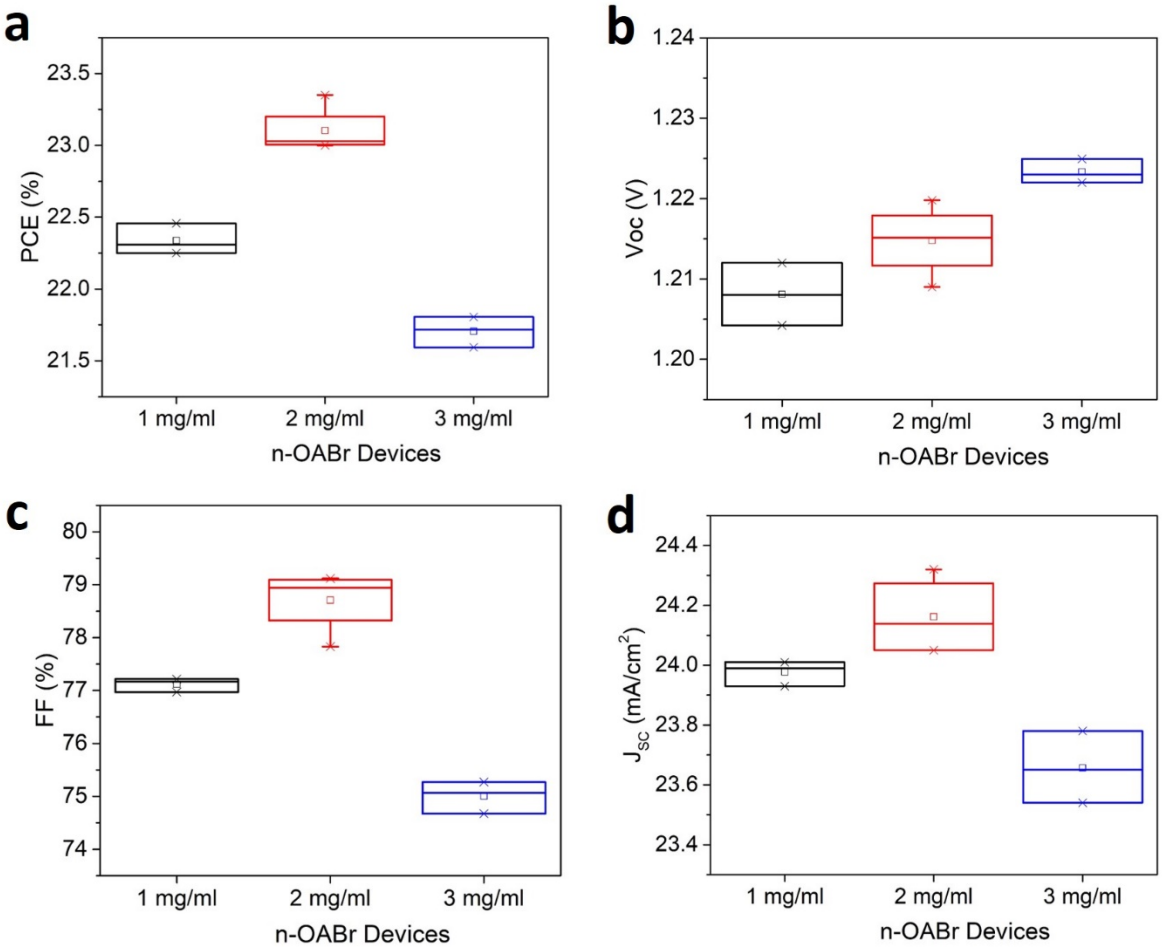

Figure S3. Statistical distribution of J-V parameters in OACl PSCs for different concentrations: a. distribution of PCE, b. distribution of V_{OC}, c. distribution of FF and d. distribution of J_{SC}

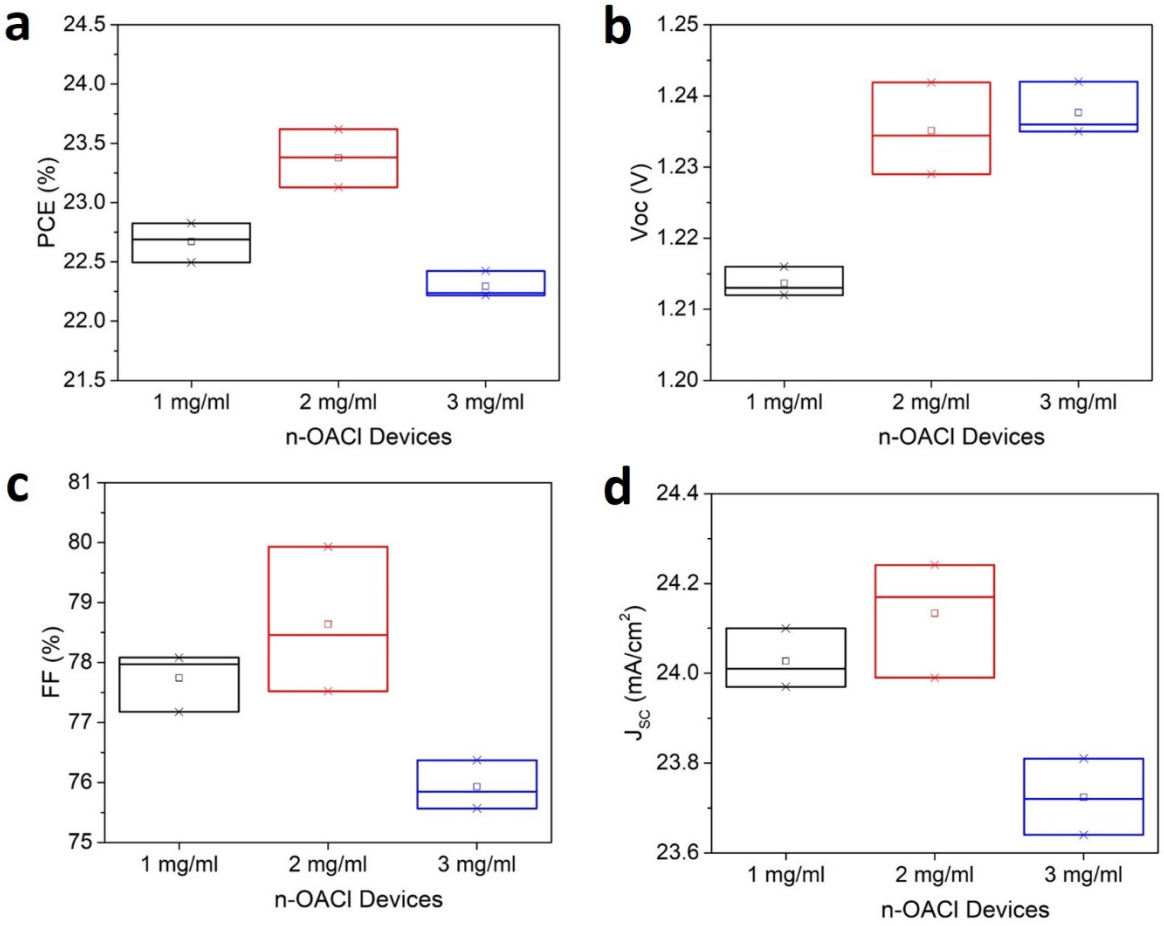

Figure S4. Cross-section SEM image of (a) control, (b) OAI, (c) OABr and (d) OACl PSCs, demonstrating the invidividual layer thickness of the thin-films.

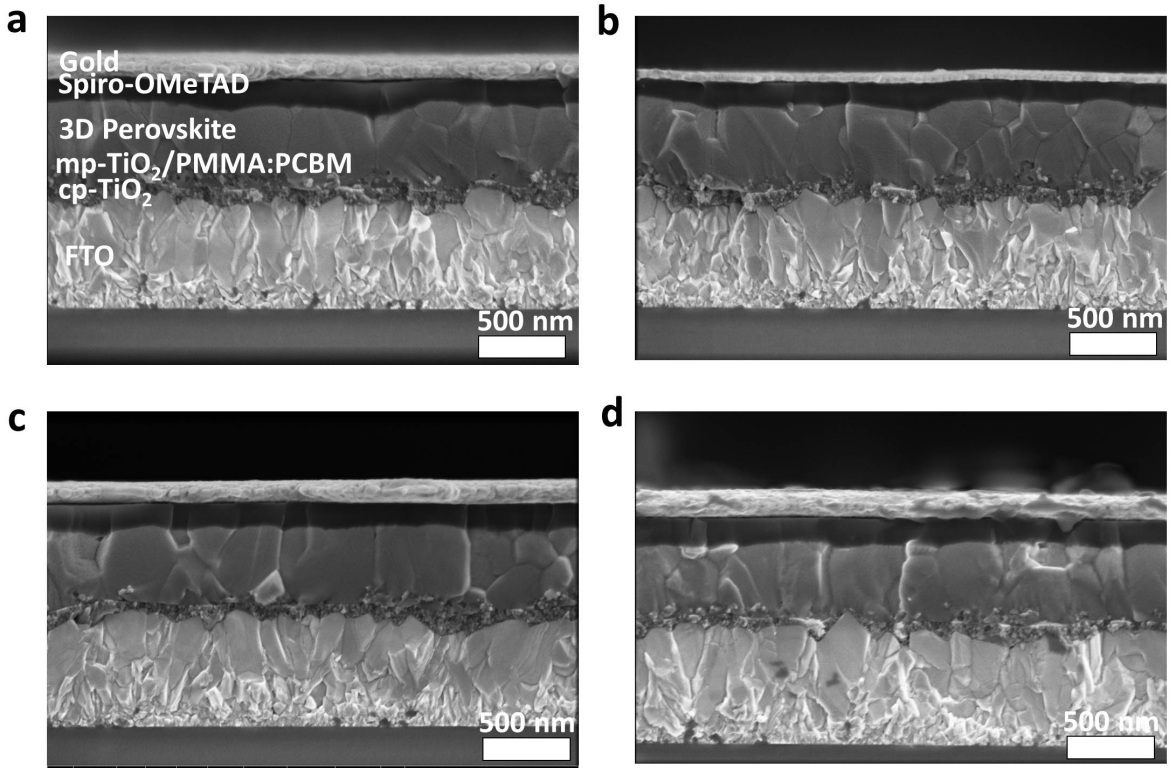

Figure S5. a. MIE spectra of control, OAI, OABr and OACl perovskite samples, b. Decomposition of MIE spectra into reference spectra using singular value decomposition (SVD) analysis and c. Weighting factor 2D and 3D (control) perovskite from SVD analysis of MIE spectra

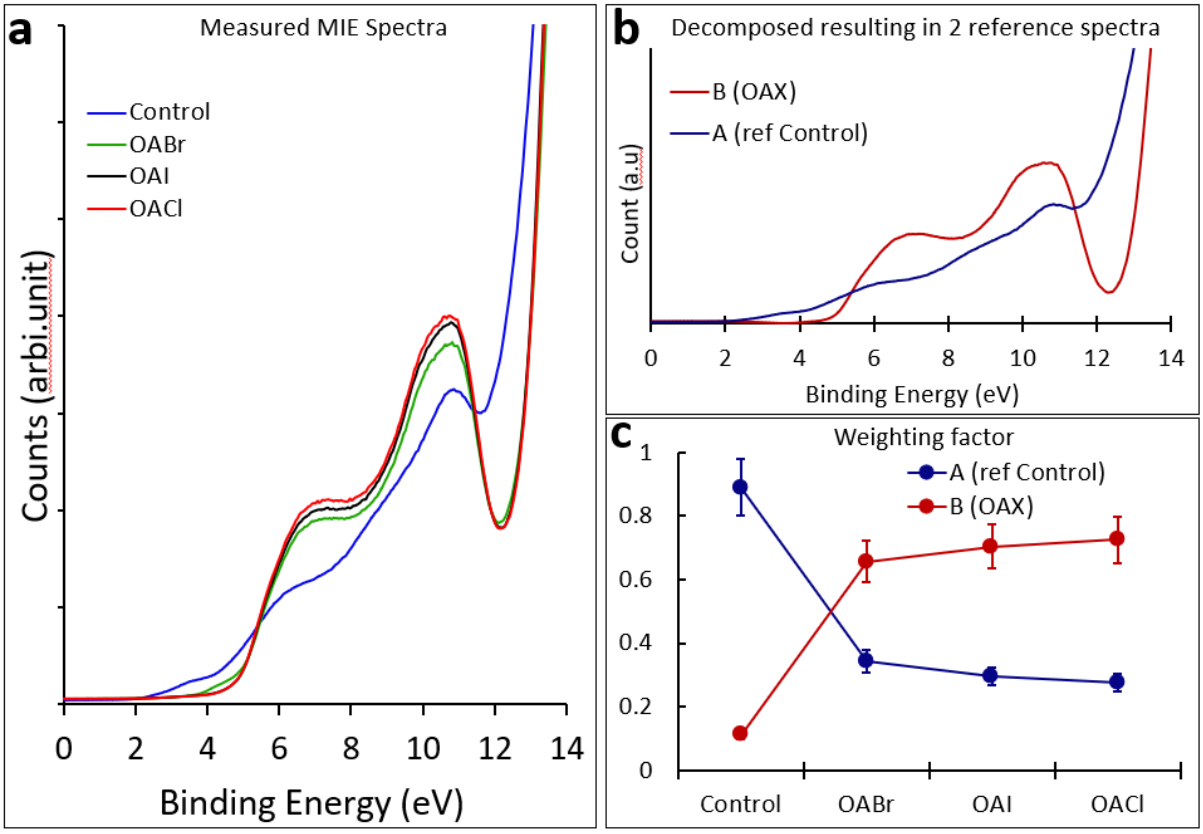

Figure S6. J-V curves of best-performing a. control, b. OAI, c. OABr and d. OACl PSCs in both forward and reverse scan directions (scan rate: 50 mV/s)

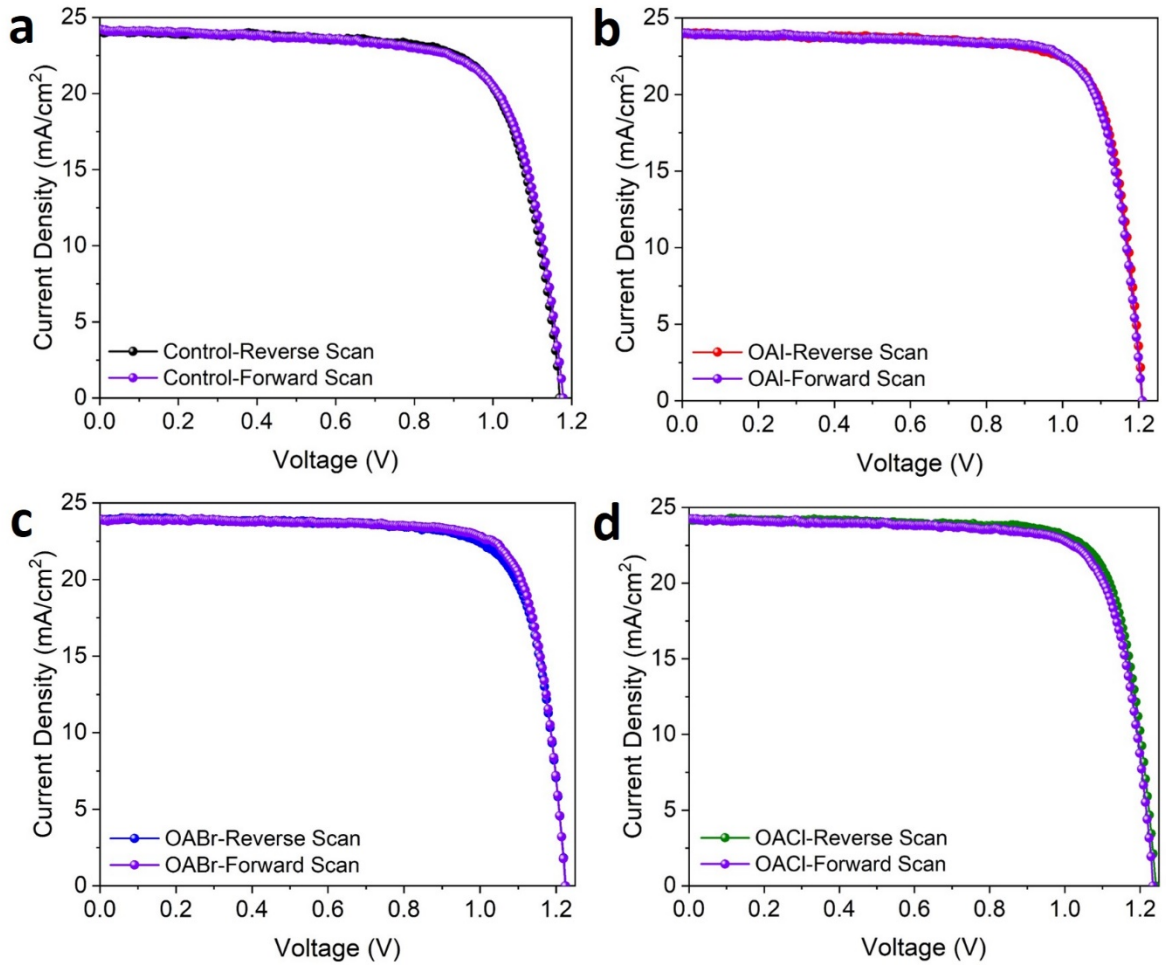

Figure S7. PL images of a. OAI, b. OABr and c. OACl PSCs under open-circuit condition for precursor concentration of 3 mg/ml

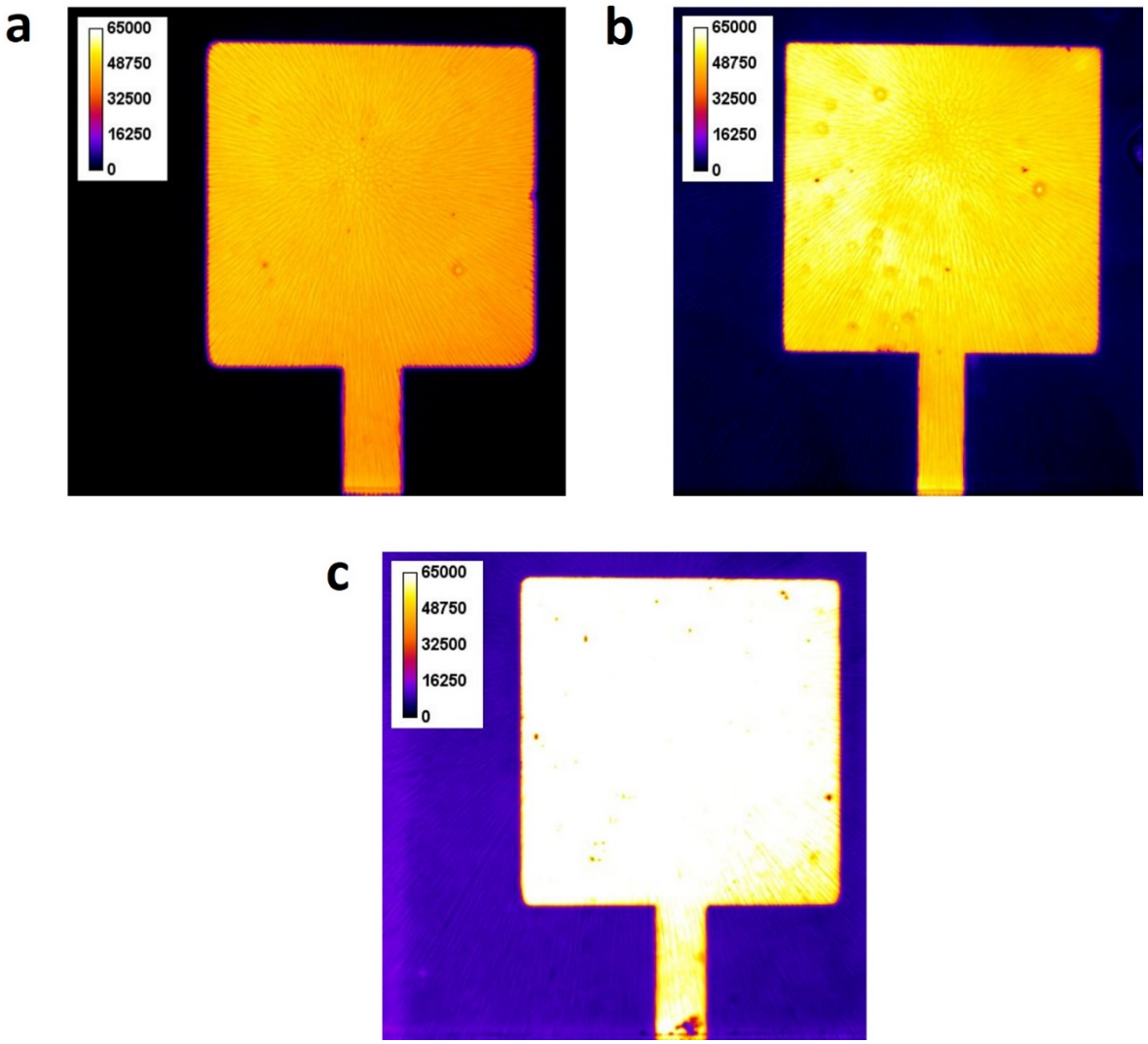

Figure S8. Deconvolution of high-resolution (a) C 1s and (b) N 1s XPS spectra for all perovskite films

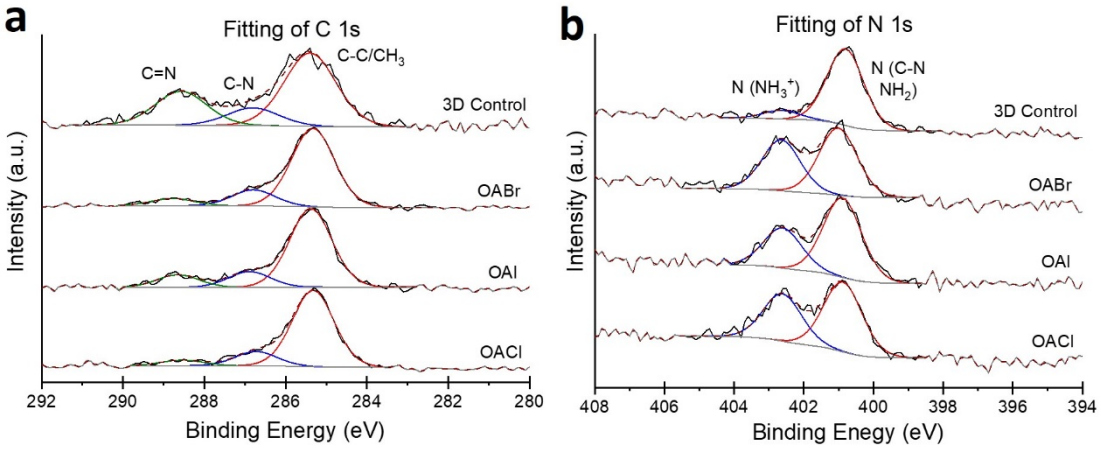

Figure S9. SEM Surface morphology images of a. Control, b. OAI, c. OABr and d. OACl perovskite films

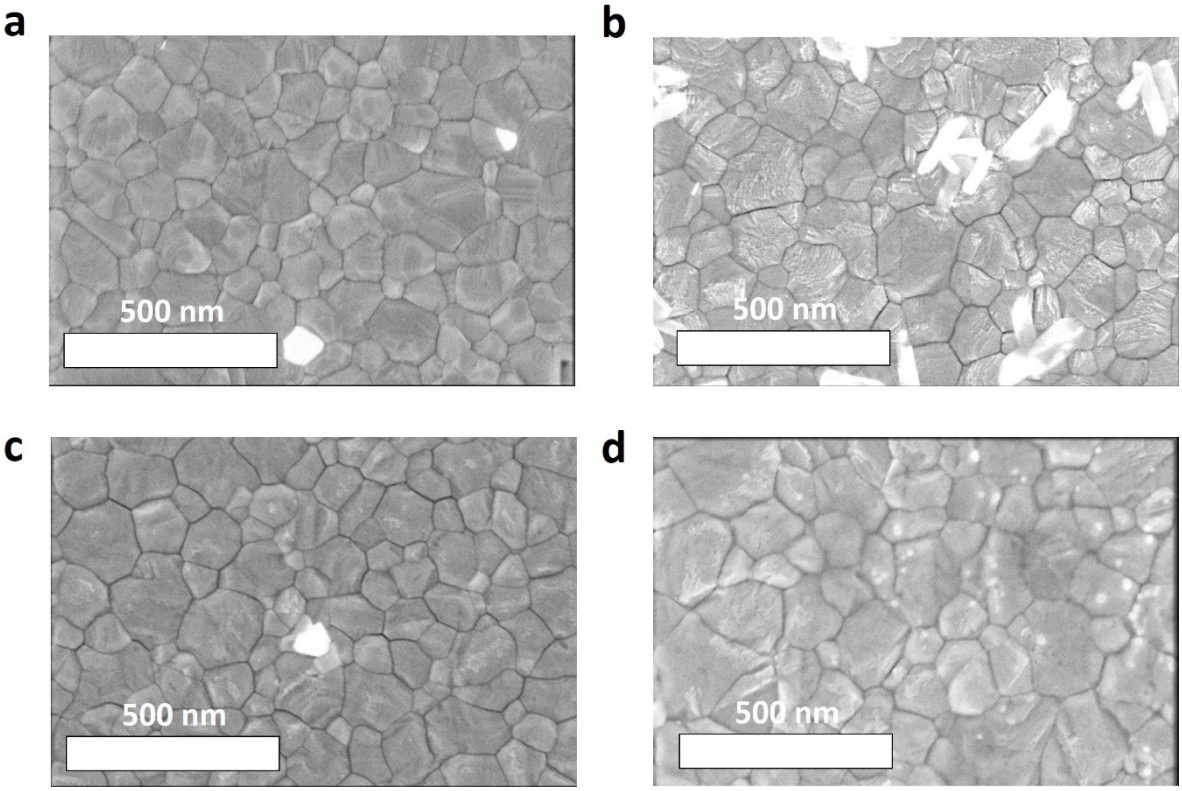

Figure S10. Absorbance curves of control, OAI, OABr and OACl perovskite films (the inset shows the band-edge of the absorbance curves)

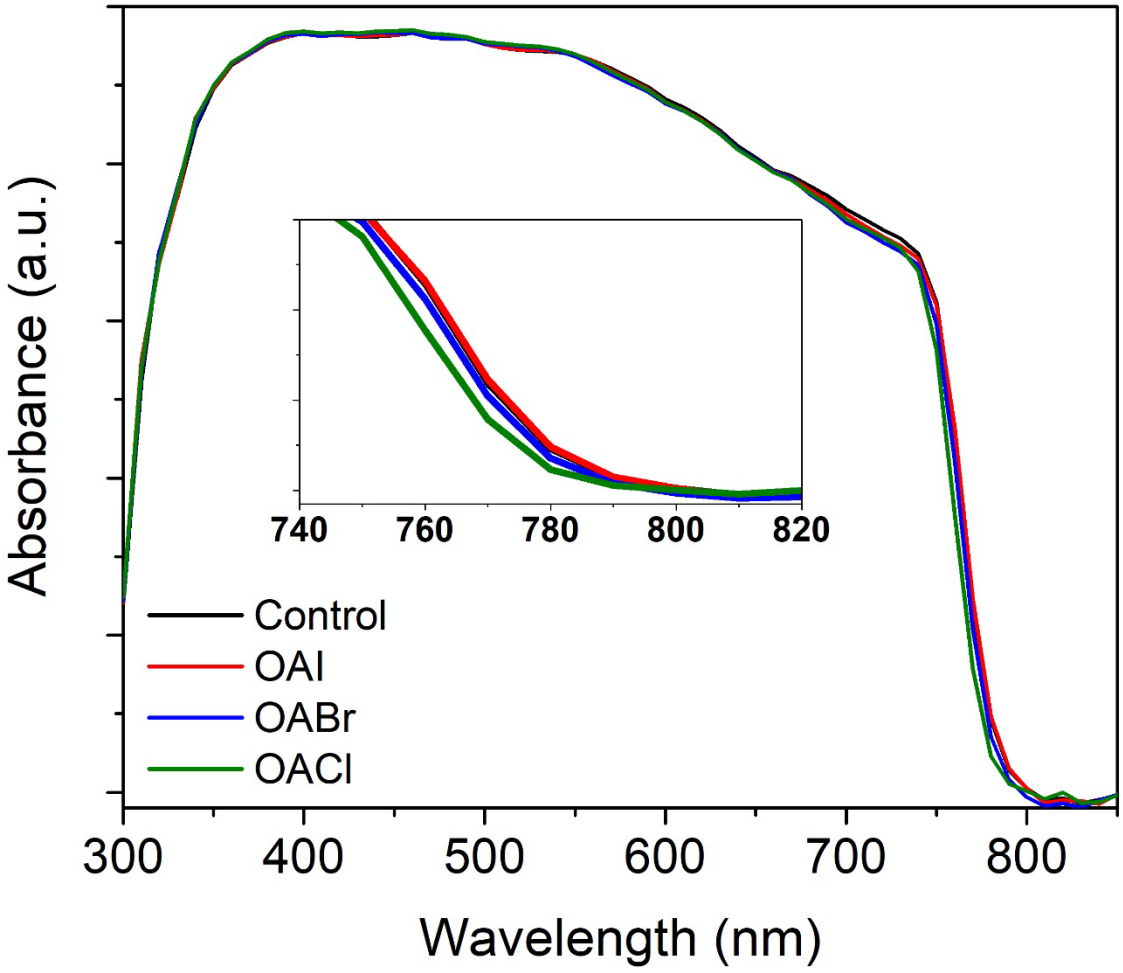

Figure S11. (a, b, c) Absorbance patterns and (d, e, f) Tauc plots of OAI, OABr and OACl perovskite films for different precursor concentration of spacer-cation compounds

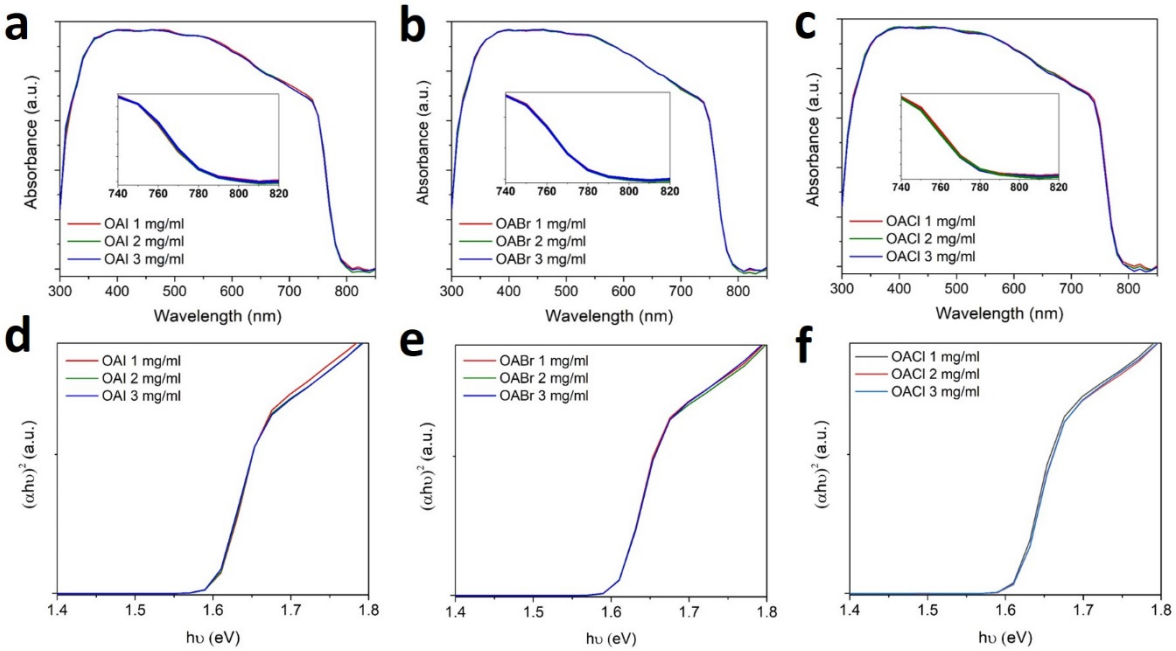

Figure S12. SEM-EDX mapping image of control perovskite surface, demonstrating the distribution of different elements on the relevant perovskite film

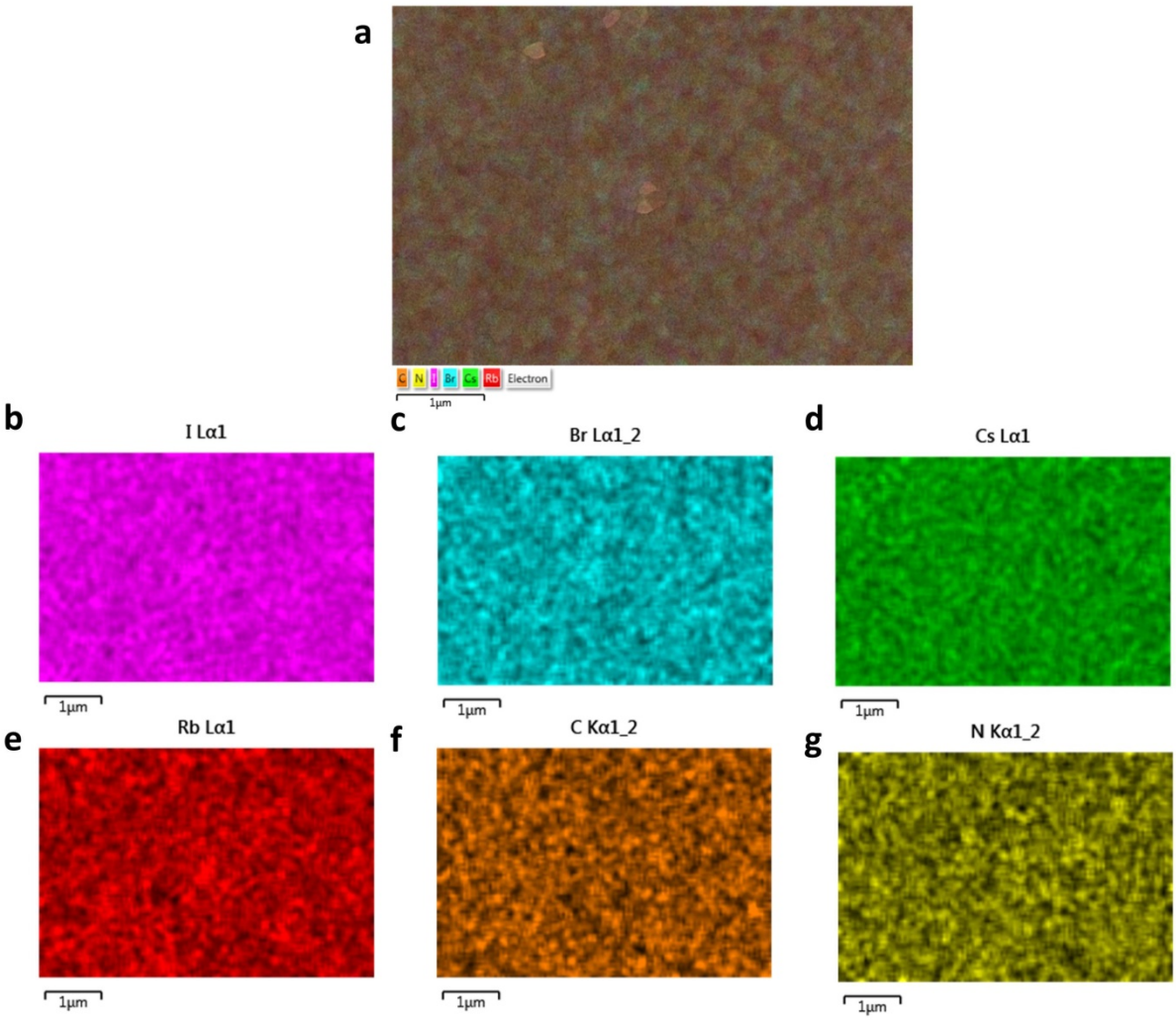

Figure S13. SEM-EDX mapping image of OAI perovskite surface, demonstrating the distribution of different elements on the relevant perovskite film

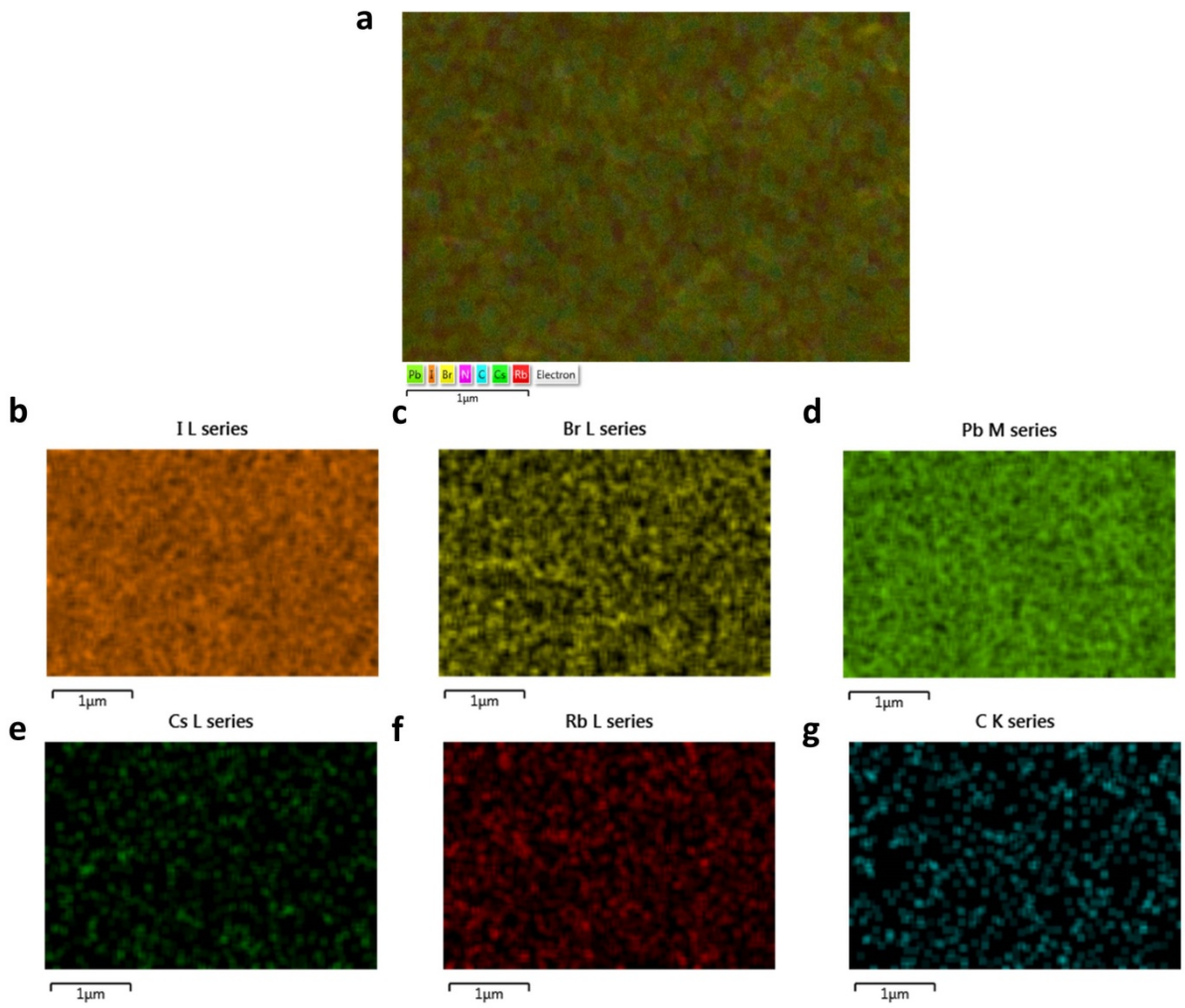

Figure S14. SEM-EDX mapping image of OABr perovskite surface, demonstrating the distribution of different elements on the relevant perovskite film

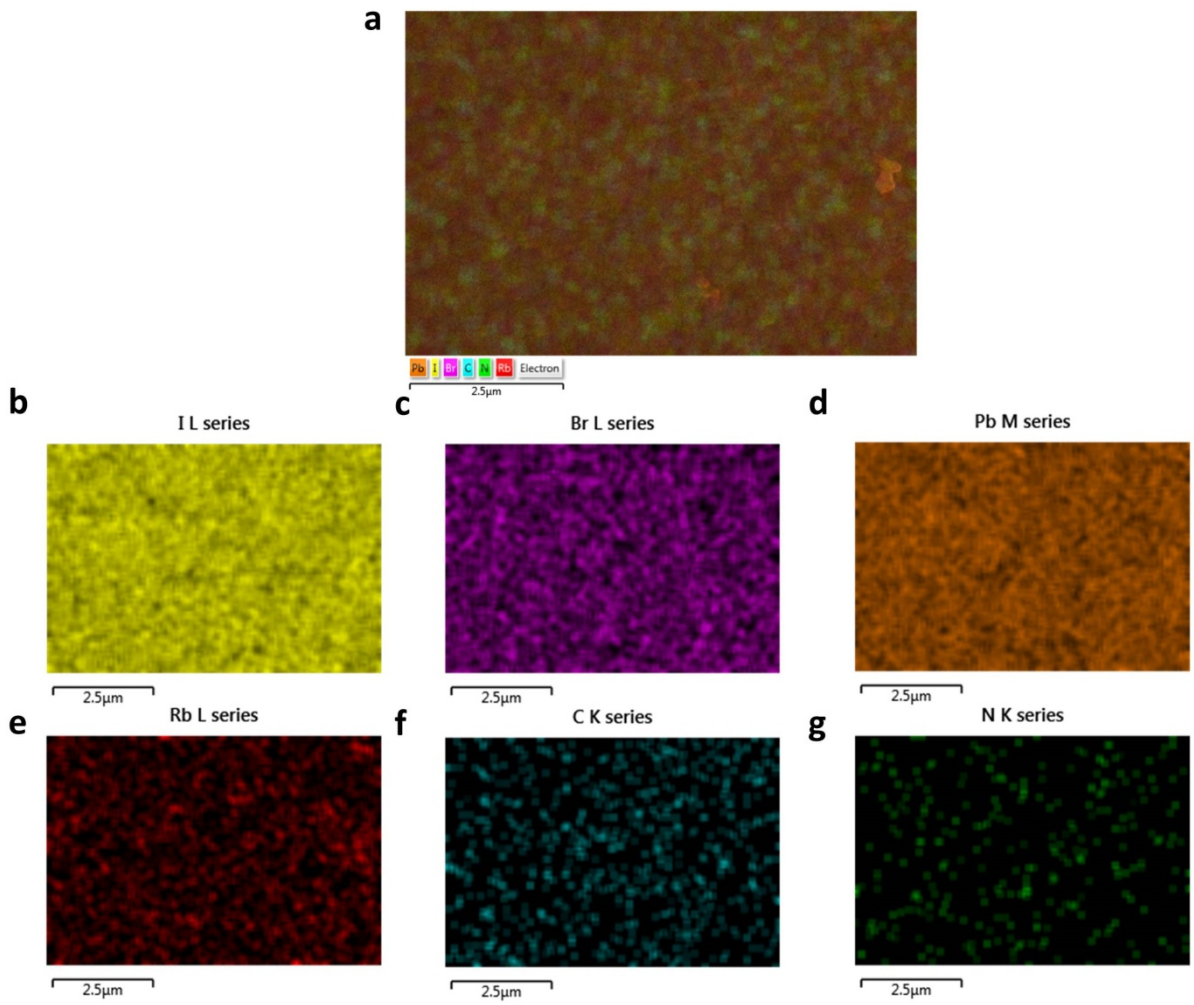

Figure S15. Angle-resolved XPS of a. Control, b. OAI, c. OABr and d. OACl perovskite films to show the distribution of element outer surface layer (up to 10 nm from surface) of the perovskite films

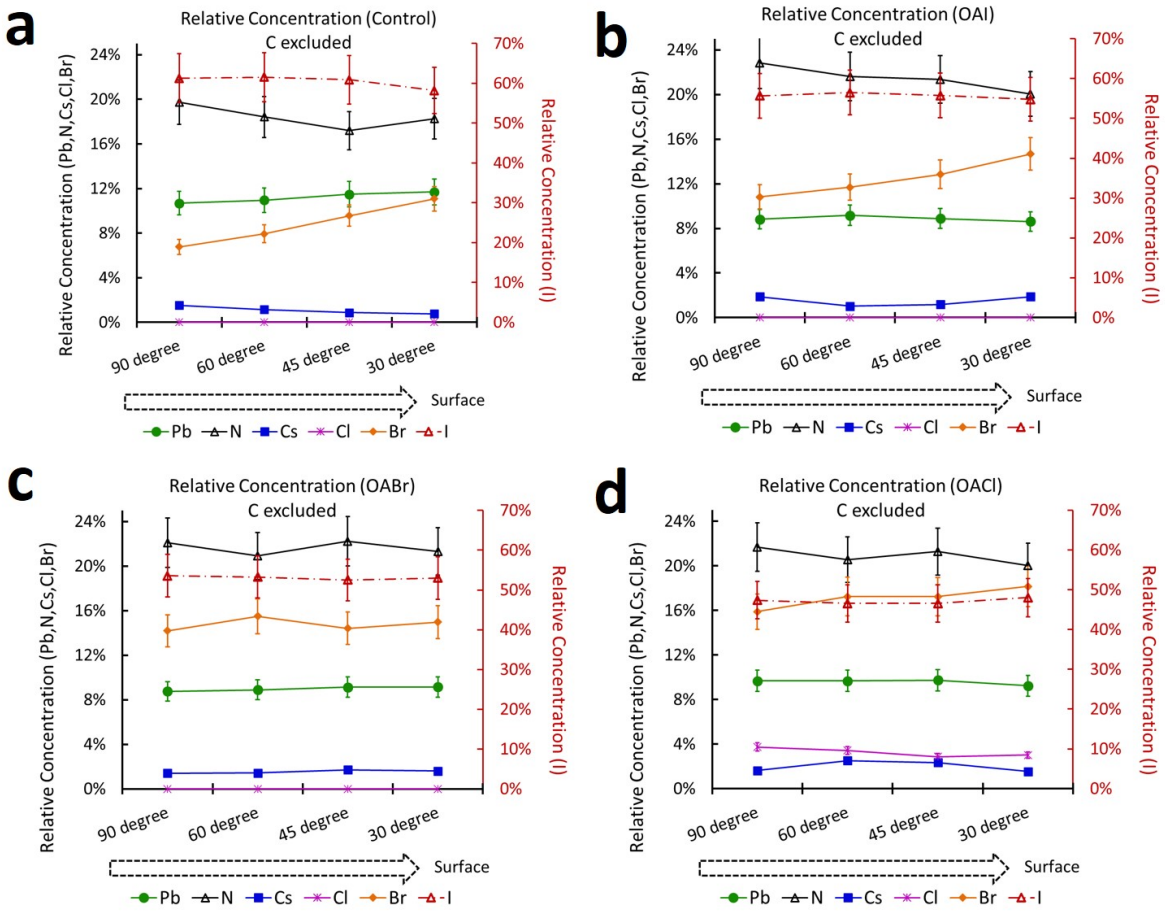

Figure S16. Cross-section SEM-EDX mapping image of control device, demonstrating the distribution of elements at different thin-film layers of the device

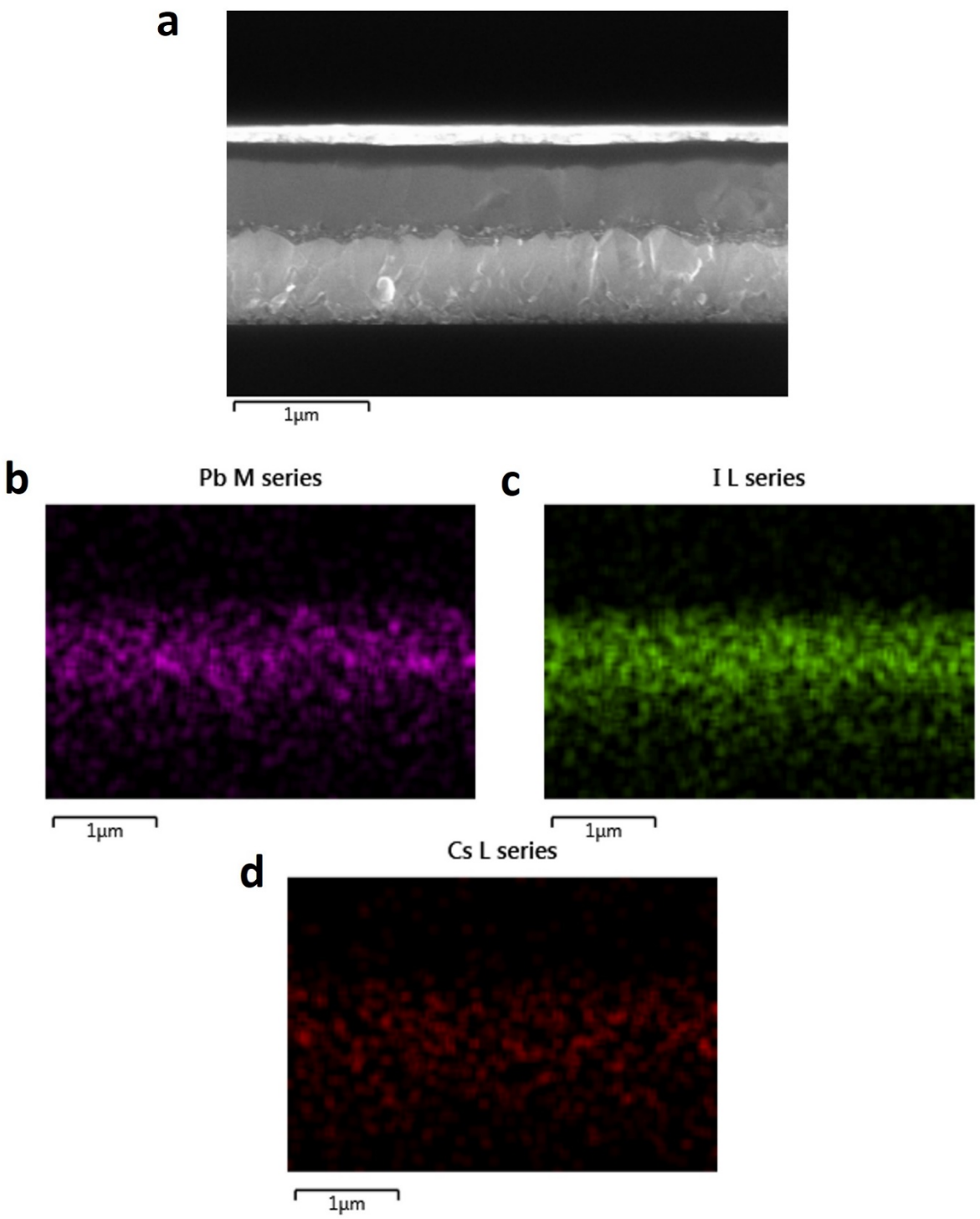

Figure S17. Cross-section transmission electron microscopy (TEM) image of unannealed OACl device, (a) full cross section, (b)-(c) higher magnification image showing the 2D perovskite is not clearly visible in unannealed sample as compared to annealed sample at 3D perovskite/HTL interface, (d) higher magnification image showing characteristic interplanar spacing of 2D and 3D perovskite at a very small region which indicates 2D perovskite formation is not complete in the unannealed sample

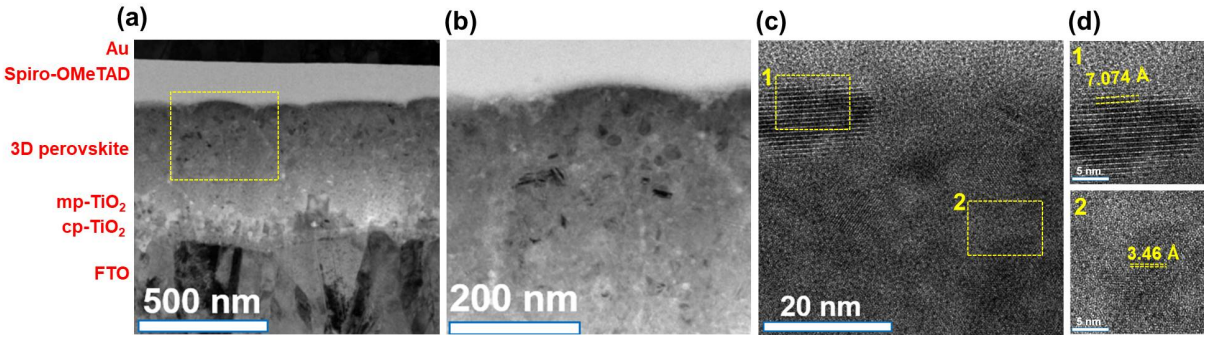

Figure S18. Cross-section SEM-EDX mapping image of unannealed OACl perovskite device, demonstrating the distribution of elements at different thin-film layers of the device

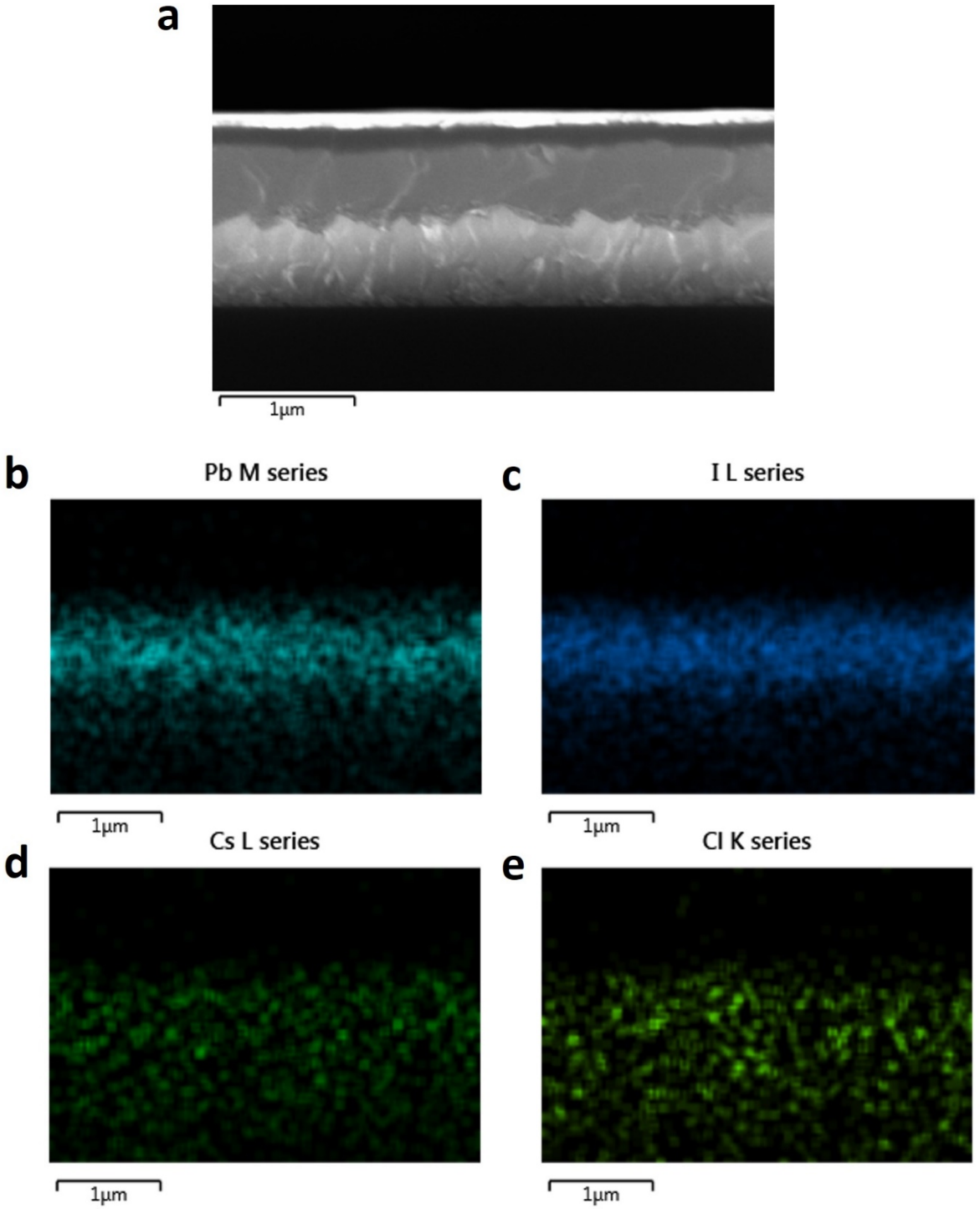

Figure S19. Light-soaking stability data of control, OAI, OABr and OACl PSCs under an inert condition for 70 hours

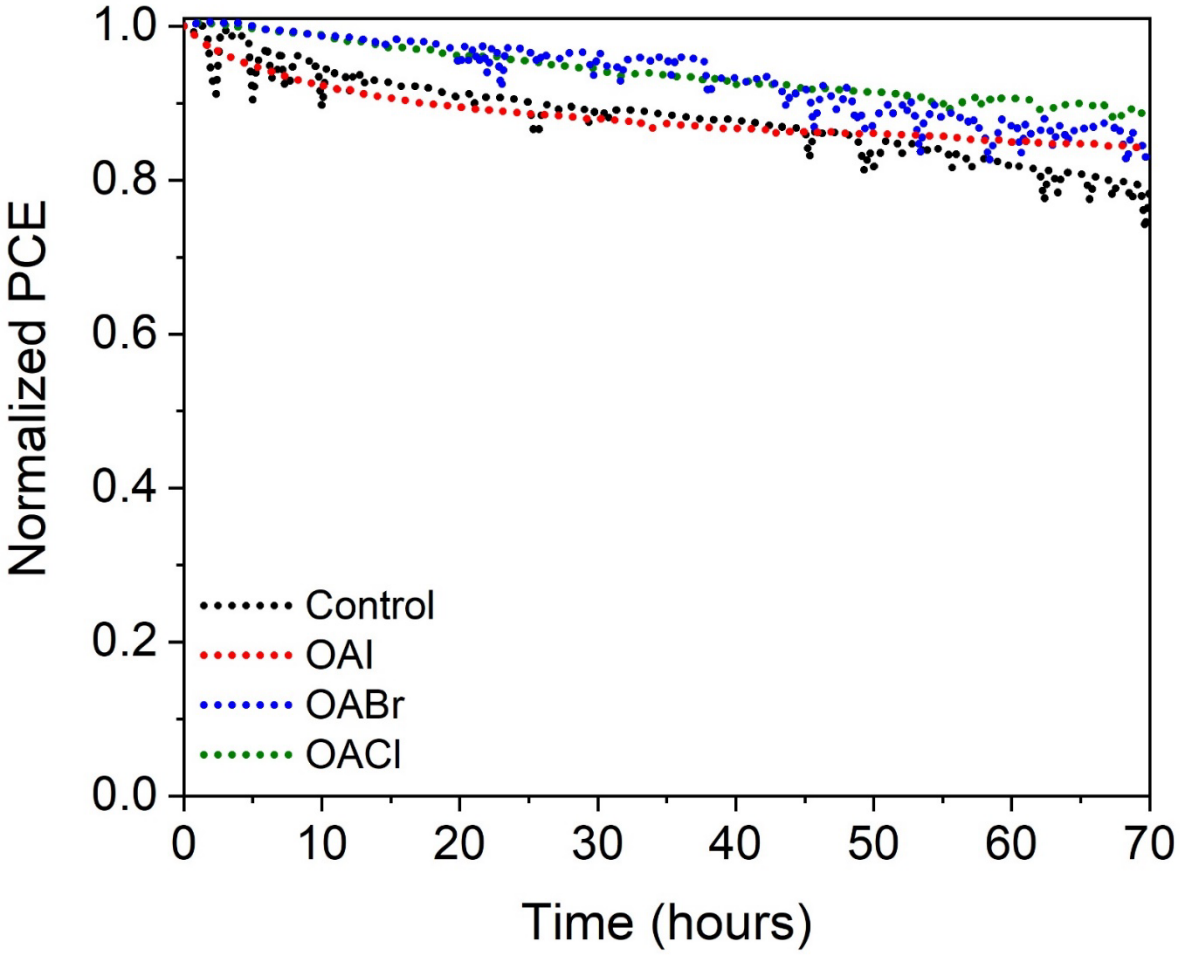

References:

[1] Peng, J.; Khan, J. I.; Liu, W.; Ugur, E.; Duong, T.; Wu, Y.; Shen, H.; Wang, K.; Dang, H.; Aydin, E.; Yang, X.; Wan, Y.; Weber, K. J.; Catchpole, K. R.; Laquai, F.; De Wolf, S.; White, T. P., A Universal Double-Side Passivation for High Open-Circuit Voltage in Perovskite Solar Cells: Role of Carbonyl Groups in Poly(methyl methacrylate). *Advanced Energy Materials* 2018, *8* (30), 1801208.

[2] Peng, J.; Wu, Y.; Ye, W.; Jacobs, D. A.; Shen, H.; Fu, X.; Wan, Y.; Duong, T.; Wu, N.; Barugkin, C.; Nguyen, H. T.; Zhong, D.; Li, J.; Lu, T.; Liu, Y.; Lockrey, M. N.; Weber, K. J.; Catchpole, K. R.; White, T. P., Interface passivation using ultrathin polymer–fullerene films for high-efficiency perovskite solar cells with negligible hysteresis. *Energy & Environmental Science* 2017, *10* (8), 1792-1800.

[3] Wang, Y.; Shen X.; Arandiyan, H.; Yin, Y.; Sun, F., Chen, X.; Garbrecht, M.; Han, L,. Andersson,; G. G., Zhao, C.; Tuning the surface energy density of non-stoichiometric LaCoO3 perovskite for enhanced water oxidation, *Journal of Power Sources*, 2020, 478, 22848.

[4] Yin, Y., Sibley, A., Quinton, J. S., Lewis, D. A., Andersson, G. G. Dipole Formation at the MoO3/Conjugated Polymer Interface, *Advanced Functional Materials.* 2018, 28, 1802825.

[5] Mahmud, M. A., Duong, T., Yin, Y., Peng, J., Wu, Y., Lu, T., Pham, H. T., Shen, H., Walter, D., Nguyen, H. T., Mozaffari, N., Tabi, G. D., Liu, Y., Andersson, G., Catchpole, K. R., Weber, K. J., White, T. P., In Situ Formation of Mixed-Dimensional Surface Passivation Layers in Perovskite Solar Cells with Dual-Isomer Alkylammonium Cations. *Small* 2020, 16, 2005022.